COMPLIANT MICROJOINT

REPLACEMENTS

by

Kurtis Ross Ford

A thesis submitted to the faculty of
The University of Utah
in partial fulfillment of the requirements for the degree of

Master of Science

Department of Mechanical Engineering

The University of Utah

May 2011

Copyright © Kurtis Ross Ford 2011

All Rights Reserved

The University of Utah Graduate School

STATEMENT OF THESIS APPROVAL

The thesis of **Kurtis Ross Ford**

has been approved by the following supervisory committee members:

Ian R. Harvey	, Chair	**3/16/2011** Date Approved
Rebecca Brannon	, Member	**3/16/2011** Date Approved
Bruce K. Gale	, Member	**3/16/2011** Date Approved

and by **Timothy A. Ameel** , Chair of

the Department of **Mechanical Engineering**

and by Charles A. Wight, Dean of The Graduate School.

ABSTRACT

Contact surfaces in micromechanical pin joints, hinges, and sliders introduce stiction and friction that disrupt motion in micro-electromechanical systems (MEMS). This thesis presents compliant design alternatives that move both in-plane and out-of-plane without introducing contact interference. This document correlates experimental results from fabricated devices to numeric models developed to predict key mechanical responses. The microsystems include the following:

- A spiral cantilever spring (shaped like a watch spring) deflects out-of-plane 70% of its largest in-plane dimension. The deflection occurs because of force imparted by injected charge from a scanning electron microscope.
- Compliant beams in torsion enable motion that is similar to that of a bushing-style substrate or scissor hinge.
- A manual torsion load turns an elastic hoop inside-out as an example of a compliant bistable threshold hinge.
- A compliant linkage symmetrically translates in-plane rotary motion to radial motion, similar to a blade aperture mechanism in a camera.

These devices exemplify microsystems that avoid failure-inducing surface contact by exploiting an increase in component compliance that occurs as a result of lower bending and torsion stress response in beams with microscale cross-sections.

TABLE OF CONTENTS

ABSTRACT iii

ACKNOWLEDGMENTS vi

INTRODUCTION 1

Background and Organization of the Thesis 1

CHAPTER

1 MICROMECHANICAL CONTACT 4

1.1 Scaling Effects 4
1.2 The Hinge Problem 5
1.3 Compliant Mechanism Solution 13

2 COMPLIANT HINGES…….. 16

2.1 Torsion Springs in Parallel 17
2.2 Torsion Springs in Series 23

3 CASE-STUDY– TORSION BISTABLE MECHANISM 30

3.1 Background to Microcompliant Bistable Mechanisms 30
3.2 Modeling a Micro-Elastic Ring 31

4 CASE STUDY– RADIAL MOTION TRANSDUCER 38

5 CASE STUDY – PROBELESS SPIRAL SPRING ACTUATOR 50

6 CONCLUSIONS 58

6.1 Observations and Conclusions 58
6.2 Contributions 59

7 FUTURE WORK 61

7.1 Future Development of Compliant Roation-to-Radial Motion Transducer 61

7.2 Future Development of Bistable Compliant Hoop 63
7.3 Overview of Dynamic Charge Injection 64

APPENDICES

A: ANSYS CODE TO SIMULATE A BISTABLE ELASTIC HOOP............................70

B: LINEAR SPRING CONSTANT OF THE SPIRAL SPRING ACTUATOR 72

REFERENCES 79

ACKNOWLEDGMENTS

First, I express my deep appreciation to my advisor, Dr. Ian Harvey, for giving me the opportunity to do this research. Dr. Harvey spent countless hours patiently mentoring me and working through several design concepts. I thank Dr. Rebecca Brannon for helping me understand the fundamental concepts regarding finite element analysis, elasticity, and continuum mechanics. Dr. Brannon took extra time on numerous occasions (including weekends) to answer questions on these topics. I also thank Dr. Bruce Gale for offering hands-on guidance in microfabrication and experimental procedures.

I am grateful to Brian Baker for acting as a second advisor to me. Brian taught me the fundamentals of the SUMMiT-V™ process and helped with my designs. He willingly performed all of the manually actuated experiments in this thesis.

I appreciate Alex Hogan, who performed most of the dynamic charge injection experiments in the thesis and helped with my designs. I express my gratitude to Charles Fisher, who laid out the compliant rotational-to-linear motion transducer.

I am further indebted to numerous engineers and scientists outside of the University of Utah with whom I consulted on several occasions. They include, but are not limited to, Dr. Ed Cole, Mike Baker, Dr. Mathew Brake, and Dr. Larry Howell.

Finally, I express my heartfelt gratitude to the love of my life, Megan, who willingly accompanied and supported me in this endeavor.

INTRODUCTION

Background and Organization of the Thesis

Humankind has spent thousands of years developing and applying simple design strategies to perform useful work with machines. Recently, a new paradigm of machine design has emerged with the advent of microscale fabrication.

Micromachined devices, generically referred to as micro-electromechanical systems (MEMS), directly followed the revolution in microscale transistors. Semiconductor batch processes used to manufacture transistors employ thin layers of material that interact with one another by design. The high degree of control in thin film deposition and patterning spawned surface micromachining techniques that stack and pattern materials with strategically shaped and positioned interconnections. The resultant geometry forms 3-dimensional mechanical structures that can be given machine functionality [1,2]. The new capabilities inspired early designers to build micromachines that mimicked macroscale counterparts. Though engaging, the microsized versions of traditional machines often failed to take advantage of physics that dominate the micrometer scale. Specifically, early micromachine engineers produced microhinges and pin joints that were merely scaled-down versions of ordinary macromachine components; in practice, microjoints demonstrate failure modes resulting from high surface-area contact and poor machining tolerance.

This thesis describes the conceptual basis for MEMS design that avoids pitfalls of downscaling hinged joints. In preference, it suggests the use of compliant structures that take advantage of beneficial physical laws dominant at the microscale. The document organization is as follows:

- Chapter 1 describes how certain physical laws dominate at different scales. The chapter explains the fundamental problems with mechanical hinges and pin joints derived from scale-specific and microfabrication-process constraints. Furthermore, it recommends taking advantage of the increase in beam compliance on the microscale to eliminate hinges and pin joints.
- Chapter 2 showcases two out-of-plane compliant hinge experiments. The experiments show that series-beam and parallel-beam configurations can be used to provide the same motion as a microhinge.
- Chapter 3 describes turning an elastic hoop inside-out as a new compliant threshold hinge. A nonlinear finite element model finds the torque required to flip an elastic polycrystalline hoop inside-out. Artificial damping is needed to approximate snap through. Manual loading identifies the stability points of the elastic hoop and proves that it is bistable.
- Chapter 4 presents a compliant rotational-to-linear motion transducer in response to the problems associated with a microscale rigid body linkage. The motion predicted by a nonlinear finite element beam model is validated by experimentation.
- Chapter 5 describes a case study of an out-of-plane spiral spring actuator that does not use rigid body linkages.

- Chapter 6 concludes that all of the devices presented here undergo controlled displacement without hinges or pin joints. It states that microcompliant beams repeatedly twist 90° out-of-plane without a bushing, a microcompliant elastic hoop is bistable, a compliant arc attached to a ring gear translates limited tangential motion to radial motion, and a spiral spring actuator deflects 70% of its largest lateral dimension.
- Chapter 7 poses questions inspired by observations made in the experiments. It outlines design obstacles for future development of the elastic motion transducer and bistable elastic ring. In the context of these experiments, it examines observations and questions raised while implementing the dynamic charge injection technique.

CHAPTER 1

MICROMECHANICAL CONTACT

1.1 Scaling Effects

The size and shape of an object influences how it interacts with its environment. A baseball falls faster than a piece of paper because the force from air resistance is much higher on the piece of paper than the ball. Fluid resistance depends on surface area and dominates objects with large surface-to-volume ratios, such as the piece of paper. Articulating this seems trivial because our intuition takes into account the effects of surface-to-volume ratios in macro settings. One must extend this worldview to small objects that have higher surface-to-volume ratios than large objects of the same geometry. For example, a planet has a smaller surface-to-volume ratio than a bead with the same geometry. Physical laws that depend on surface area such as electrostatic attraction, surface tension, friction, fluid drag, and radiative heat transfer dominate the behavior of the bead; while physical laws associated with volume or mass density (e.g., gravity, inertia) dominate planetary motion. The dominance of certain physical laws at different magnitudes of dimensional scale is referred to generically as "scaling effects."

Dominant surface physics unique to the micrometer scale can affect micro-electromechanical systems positively or negatively. Beneficial use derives from designing microsystems to sense and actuate with the phenomena that dominate at such

scales. For instance, a microscale spring/mass system is more sensitive to acceleration changes than an equivalent macroscale device because small beams deflect more relative to their length than large ones [3]. This is important in the implementation of acceleration sensors. In an accelerometer, a conductive spring suspends a conductive mass over an electrode relative to which it is electrically biased. The relatively small proof mass corresponds to low inertia that leads to responsive trajectory changes under small accelerations. The inertial response induces relatively large beam deflections that change electrode spacing and create easily measured capacitive[1] differences [1, 3].

Conversely, microscale phenomena may jeopardize the practicality of a MEMS device if not controlled, or even eliminated from the system. If the mass in an electrostatic accelerometer comes too close to the ground plane, the corresponding increase in capacitive force overpowers the elastic restoring response holding the mass motionless [1,2]. In some cases, parasitic, or undesired, microscale phenomena dominate to such an extent that they render a microdevice inoperable. Microhinges and pin joints exemplify such components. The following sections explain how microhinges and pin joints jeopardize microsystem functions.

1.2 The Hinge Problem

In 1992, Pister introduced the first out-of-plane micromechanical hinges which extended the surface micromachining paradigm to out-of-plane structures [4,1]. Figure 1

---

[1] Capacitance between parallel electrodes is proportional to separation distance

[2] The Coulomb friction force from an interference fit is 10^6 times larger on the microscale than it would be

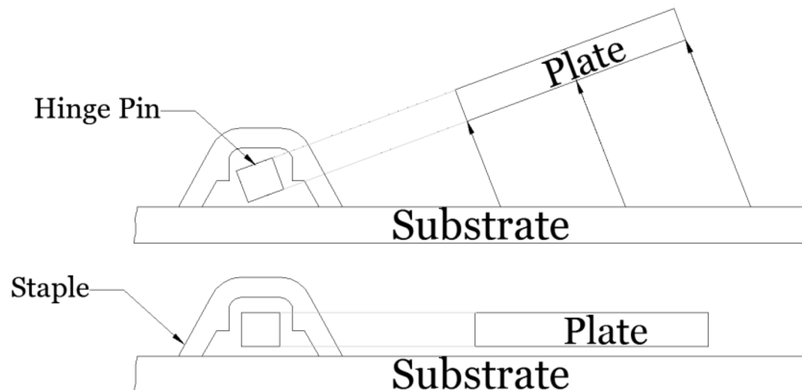

Figure 1. Diagram of Pister's hinge reconstructed from [4]. The side view at left demonstrates the binding mechanism intrinsic to the patterning methodology. Sharp corners formed during isotropic etching of the hinge bind against artifacts of conformal sacrificial coating inside the bushing. Poor machine tolerance is also evident (50-100% of the width of the pin, and typical of micromachining techniques), leading to binding from uneven application of force. At the right is an isometric view of the hinge.

shows a cartoon describing Pister's substrate hinge that constrains a floating beam to the substrate with a polycrystalline staple. In the same paper, Pister also published two scissor hinge designs that allow plates to twist relative to each other and free of the substrate. In all three cases, the thickness of the sacrificial layer between the staple and its pin before release limited the tolerances and shape of the designs to square pegs in oversized square (at best) holes.

Sandia provides similar microhinges as drop-in components in the student alliance design competition [5]. The drop-in hinges constrain a one-micron wide beam between two plates, three microns apart (Figure 2). Like other surface micromachined hinges, Sandia's fabrication process restricts their hinge geometry to a square pin in a loose-fit bushing cavity. Together, the large tolerance and square geometry expose the hinges to binding.

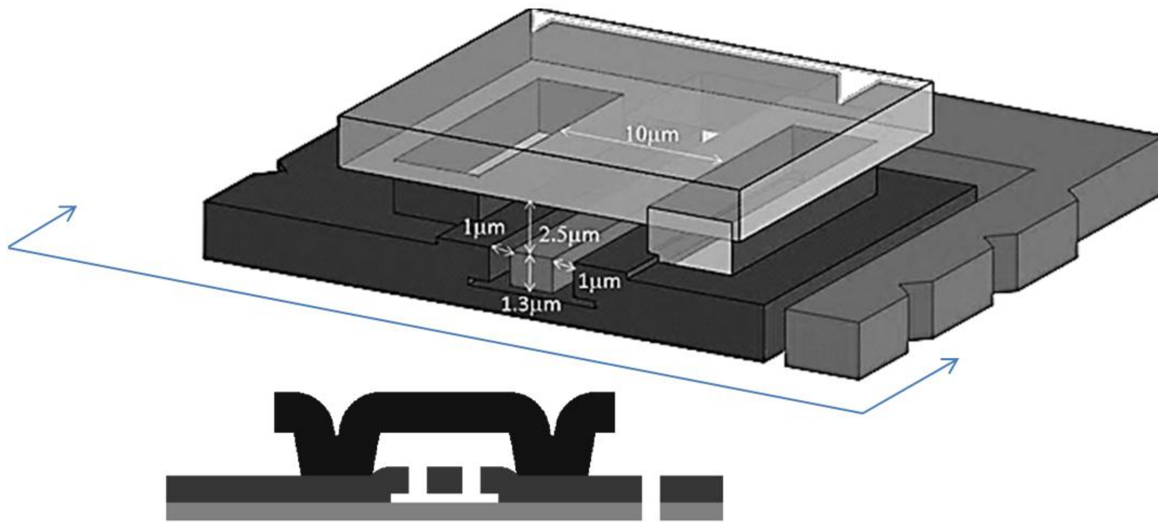

Figure 2. Dimensions of Sandia's substrate hinge. The scaled model shows that the same binding mechanisms are still present. Subject to the ability to deposit and pattern small features, all microfabrication processes result in poor machine tolerances and sharp corners[5,6].

Poor machine tolerance and square features are not the fundamental problems of a micromechanical hinge. No matter how small the tolerance or ideal the shape, a mechanical hinge pin is in frictional contact with a bushing. For example, in Sandia's surface micromachining process, pin joints that act in-plane use a round flanged pin in a round hole. The cross section of the pin joint in Figure 3 shows that the 1 μm pin has less than 0.5 μm between it and the sidewall bushing. The pin joint does not have the geometric interference issues associated with hinges that act out-of-plane; however, it is in frictional contact. Friction scales poorly on the microscale[2].

[2] The Coulomb friction force from an interference fit is 10^6 times larger on the microscale than it would be on an equivalent macro device [3].

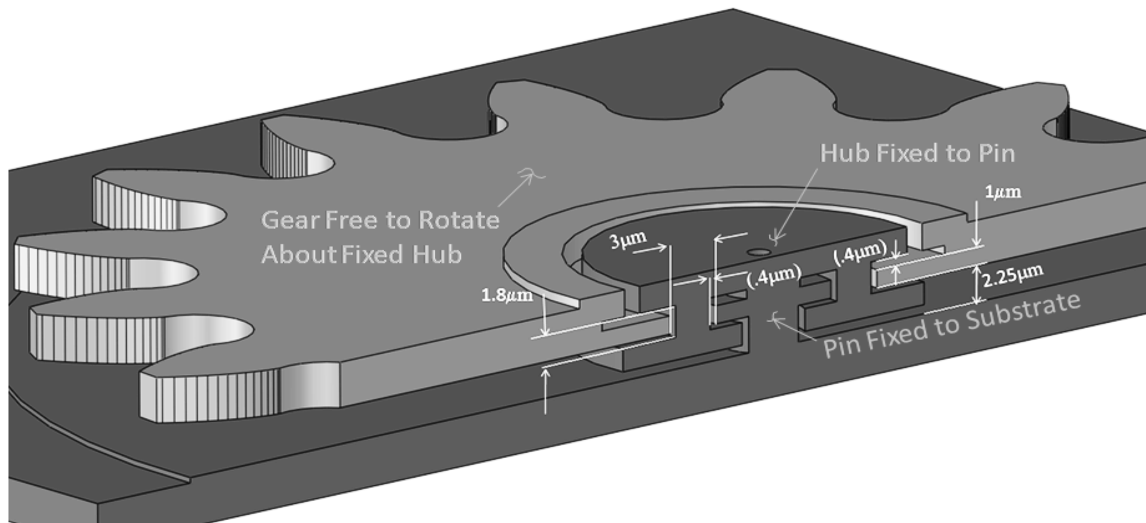

Figure 3. In-plane pin joint [5,6]. In this cross-section, the gear is free to rotate about the fixed pin. Frictional contact between the hub and gear is inevitable. Friction is a surface-dominant effect magnified on the microscale.

Surface micromachine processes generate rough surface finishes that exacerbate friction [3]. Figure 4 shows a scanning electron micrograph of polycrystalline silicon surfaces with process artifacts that occur intrinsically due to the nature of the deposition and etch processes. The imperfections of the process artifacts stem from large grain sizes relative to the dimensions of the component as well as the curtaining effects from anisotropic etching.

In addition to friction when two surfaces come into contact, capillary, electrostatic, and Van der Waal forces can dominate and often overpower the restoring force of a mechanism in a phenomenon called "stiction" [3, 9,10] (analogous to microscale static friction). In Figure 5, a micro-electroscope [10] stands out of plane though it is not being actuated. The device rests in this unnatural position because stiction adheres a microhinge and a pin joint to their bushings.

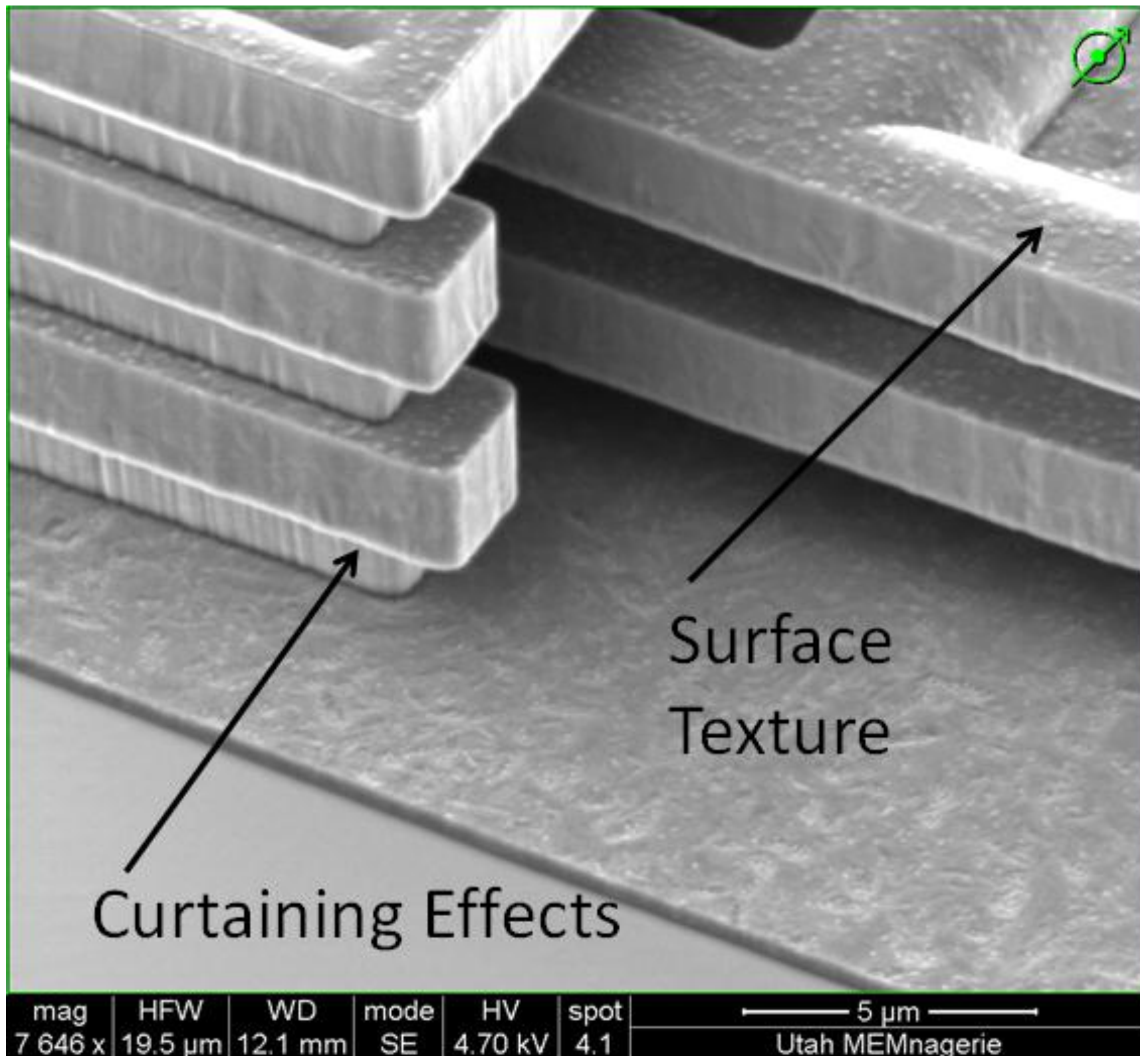

Figure 4. Textured MEMS surface. The micrograph reveals surface protrusions in the deposited polycrystalline surface. Curtaining effects on the sidewalls increase friction in the gears and hubs.

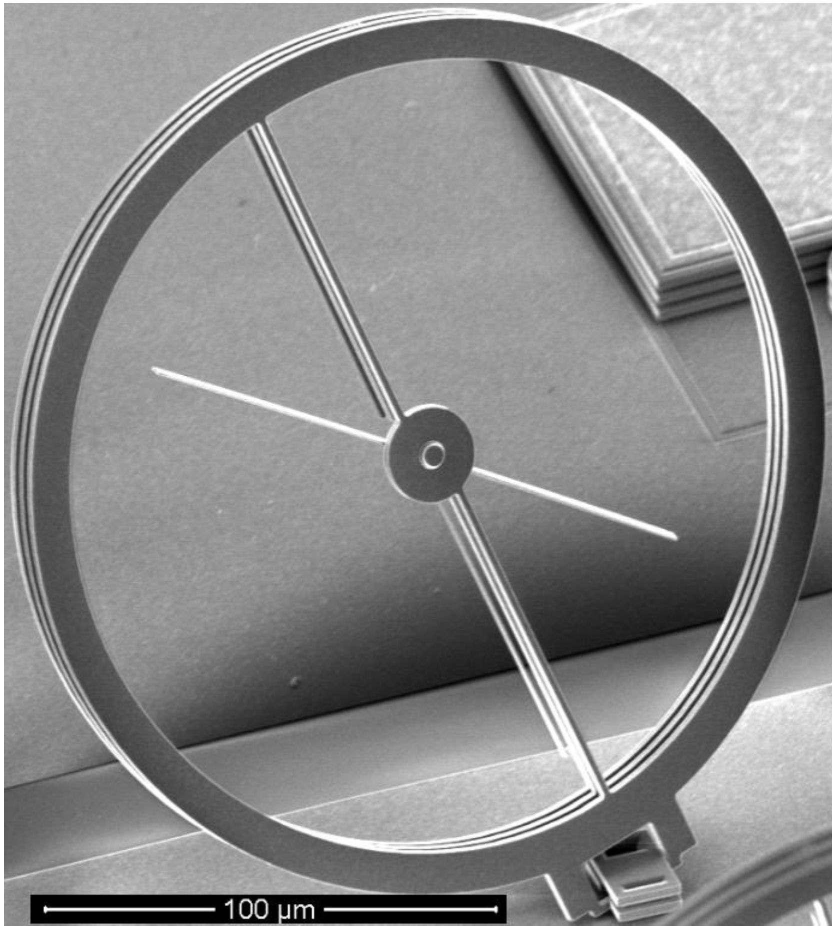

Figure 5. Example of hinge binding in MEMS application. In a dynamic charge environment, the electroscope stood out-of-plane. After actuation, both the hinge and pin joint did not lie down due to cocking of the hinge pin inside within the loose tolerance of the bushing.

In complex systems full of sliders, pin joints, or hinges, unpredictable combinations of friction and stiction slow response time, create energy losses, and disrupt motion. For instance, in 2006 the University of Utah [12] designed a micro in-plane linkage device that mimics a Hoberman linkage in two dimensions. This linkage mechanism, shown in Figure 6, uses rigid linkages, pin joints, and sliders to translate an in-plane torque from an electrostatic comb drive actuator to a radial force [13,14]. Two of the pin joint slider components are shown in Figure 7.

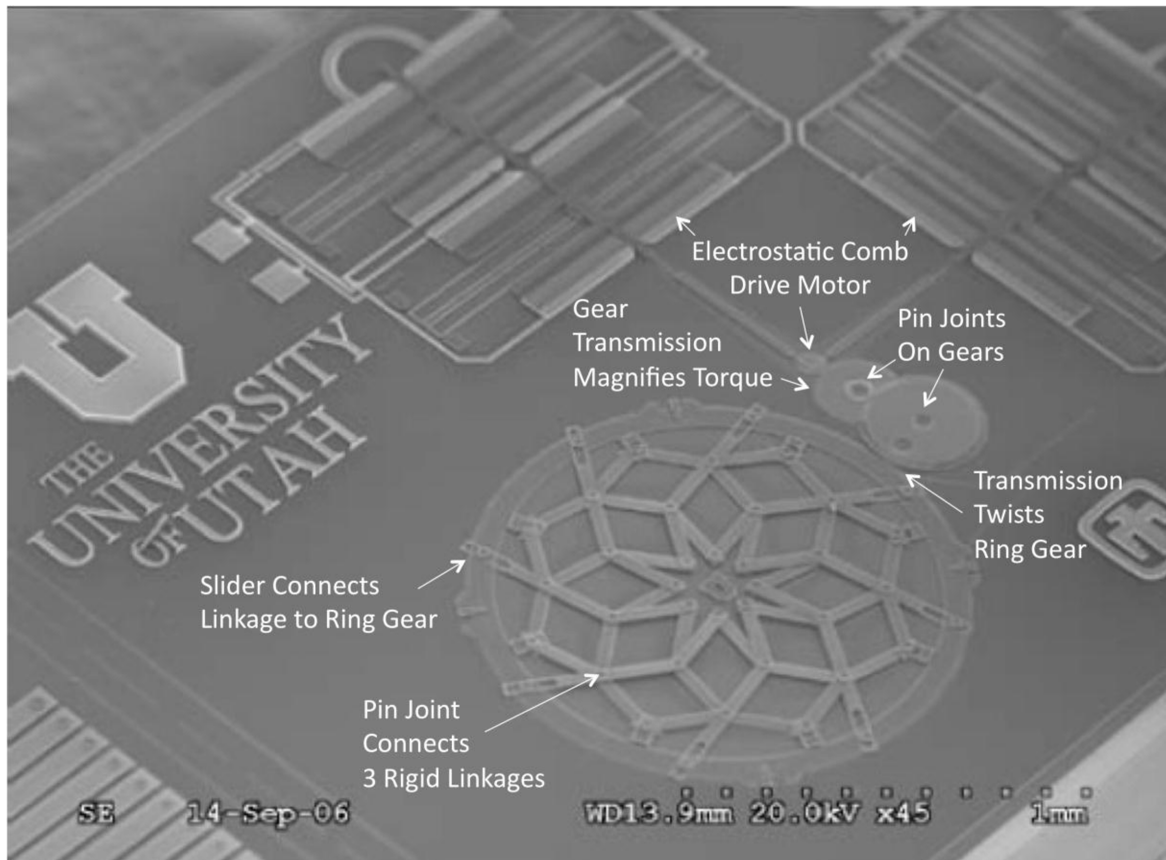

Figure 6. Example of pin joints and sliders preventing MEMS motion. Radial motion transducer linkage attached to an actuator [13,14]. Rigid links are attached to each other with micro pin joints, and to a ring gear with slider mechanisms. An electrostatic comb drive applies a torque to the ring gear through a transmission.

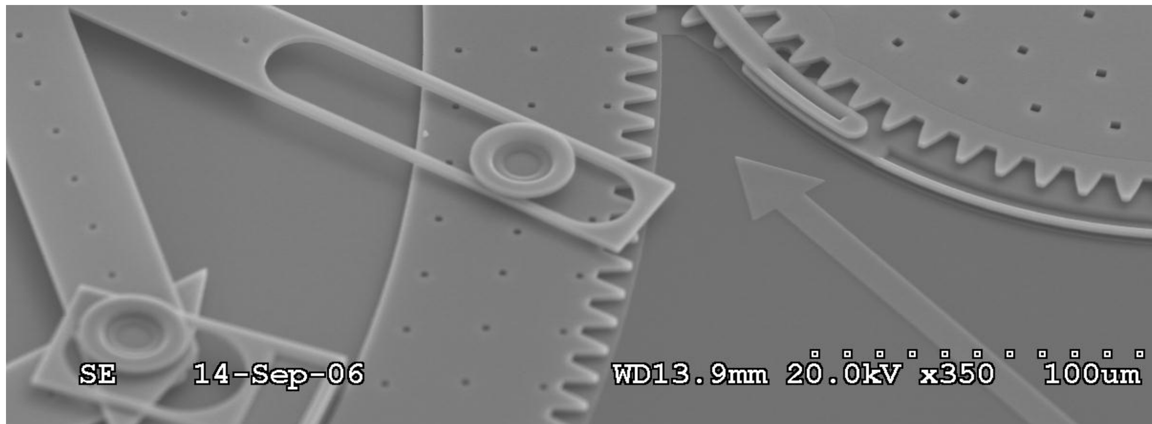

Figure 7. Slider mechanism and pin joint showing poor machining tolerance. Close-up view of the slider mechanism and pin joint show the large tolerance associated with these components.

During testing, the slider and pin joints temporarily bind the mechanism. The electrostatic comb drive actuator eventually builds up enough torque to free the linkage whereupon it binds again. In this manner, the linkage sporadically locks as the motor moves it through its ranges of motion. In Figure 8, the linkage is shown locked in its intermediate strokes.

Despite the poor motion control, the two-dimensional micro-Hoberman linkage inspired students to design a microscale blade aperture [14,15]. However, high frictional resistance in the pin joints and sliders make it difficult to predict the needed actuation force, and the MEMS implementation did not function at all. A CAD model of the blade aperture is shown in Figure 9.

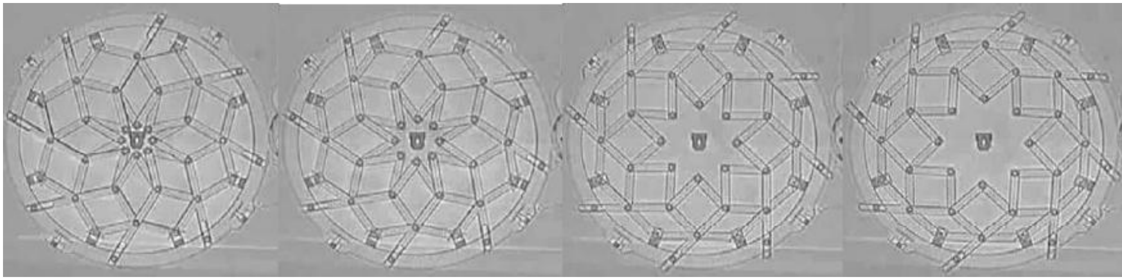

Figure 8. Radial motion transducer actuated through its entire range of motion [13,14].

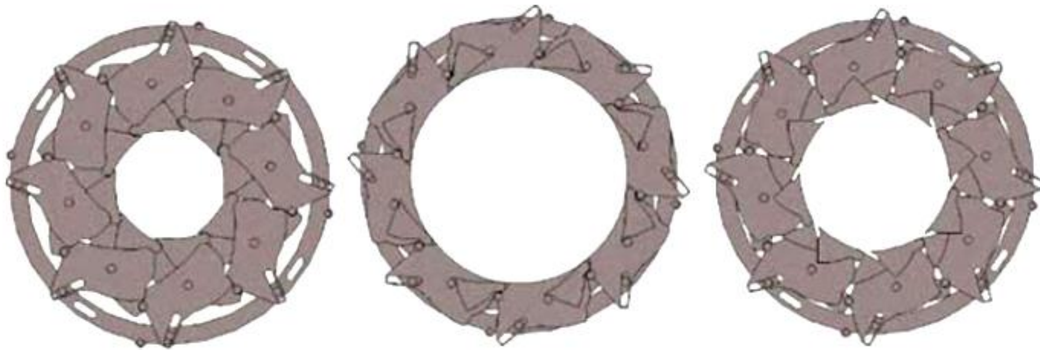

Figure 9. A microblade aperture opens and closes [15]. The MEMS implementation of this device could not be actuated at all due to the cumulative friction in all the pin and slider joints.

1.3 Compliant Mechanism Solution

Mother Nature does not use mechanical joints to create motion at the micrometer scale; she uses material compliance. Mother Nature's compliant mechanisms are flexible structures that translate motion through energy-efficient elastic deformation [16]. Compliant mechanisms work well on the microscale because small dimensions reduce bending and torsion stiffness allowing larger relative elastic deflections [3,16,17]. Nature demonstrates this principle in microorganisms that are compliant invertebrates [16,17].

For instance, tiny chlorophytas (green algae) use two compliant flagella for propulsion through a fluid [18]. The beam-like flagella use a compliant matrix of proteins ideally suited to elastic deformation [19]. The flagella also benefit from the fact that the elastic deflection of a beam is inversely proportionate to the cross-sectional length. MEMS designers may not be able to custom engineer their material to the extent nature does, but they can use current MEMS fabrication techniques to design elastic beams with small cross-sectional dimensions that increase the relative range of elastic motion.

The MEMS process architectures used to construct micro-elastic beams employ refined elastic materials such as quartz, glass, or polycrystalline silicon (variously referred to as polysilicon, or polySi). These high-modulus materials undergo little or no plastic deformation before failure and the production techniques generate few defects that serve as stress concentrators and crack initiation sites. The material purity also minimizes elastic hysteresis [3]. Tresca's failure criterion conservatively predicts brittle failure in these materials [20]. By this criterion, the maximum shear stress of a microbeam must be less than its fracture strength (1-3 GPa for polysilicon) [1].

The micro-elastic beams that undergo large deformation experience load-stiffening and elastokinematic nonlinearities [21]. As such, elliptical partial differential equations govern the elastic motion of the flexure [16]. The nonlinear character of beam motion has provoked development of simplified design methodologies that include optimization of complex beam structures and pinned rigid body linkage models with flexible equivalents [16,21,22]. Though useful for quickly developing design concepts, these simplifications may not fully predict the behavior of a compliant mechanism. Highly flexible microbeams in microcompliant mechanisms are sensitive to buckling and

dynamic snap-through [23] that idealized design strategies may overlook. Hence, finite element analysis of the governing equations and nonlinear stability analysis [23,23,25,26] are performed in this thesis to fully characterize microflexible beams with geometric nonlinearity (large deflection).

CHAPTER 2

COMPLIANT HINGES

Two of the compliant mechanisms applied to MEMS in this paper are torsion beams that enable motion similar to that of a bushing hinge. The torsion beam deserves attention because mechanical hinges still manifest in microsystems. Hinges prevail because designers need components that generate out-of-plane motion with negligible stiffness. These designers overlook the fact that hinges do not necessarily have negligible stiffness: they have an unknown stiffness. Hence, the first two compliant mechanisms presented here demonstrate stable, linear flexure with low stiffness (less than 400 pNm) that could be used in place of mechanical hinges. The compliant hinges use straight cantilever beams in torsion arrayed in series and parallel configurations.

Both hinges were tested using dynamic charge injection, a new MEMS actuation technique under development at The University of Utah [27,28]. In these experiments, a scanning electron microscope either injects electrons or creates an electron-defficient state to induce repulsion between ungrounded but electrically connected mechanical components. Dynamic charge injection is chosen because it is capable of ranging actuation force over an order of magnitude, whilst simultaneously imaging the effects using scanning electron video micrography.

2.1 Torsion Springs in Parallel

A cantilever beam in perfect torsion rotates about the centroid of its cross-section like an ideal hinge. Loading cantilever springs in parallel provides stable and predictable motion by creating symmetric reaction loads, and stress stiffening. Though they have not been directly compared to a bushing hinge in the literature, parallel torsion springs are well understood and have been thoroughly tested for reliability in micromechanical systems [29,30].

In Figure 10, two plates are connected to parallel cantilever springs that are fixed to the substrate. The springs are surrounded by constraint blocks that prevent the spring from damage during processing. The device is designed to be repelled from the substrate by dynamic charge injection, lifting the plate and twisting the cantilever "hinge replacement."

All of the components of the prototype hinge replacement are electrically-connected conductive polysilicon. They sit on a heavily doped polysilicon pad deposited over the silicon nitride foundation in SUMMiT-V™ [5,6,31]. The conductive actuator has no electrical path to ground or to the wafer substrate. The dynamic charge injection technique imparts a load that generates a net torque about the torsion spring in Figure 11. The plate is made of two polysilicon layers connected at the point where they fasten to the spring. The bottom plate has slots that amplify the actuation force by increasing the exposed surface area. The dimensions of the actuator and spring are given in Figure 12.

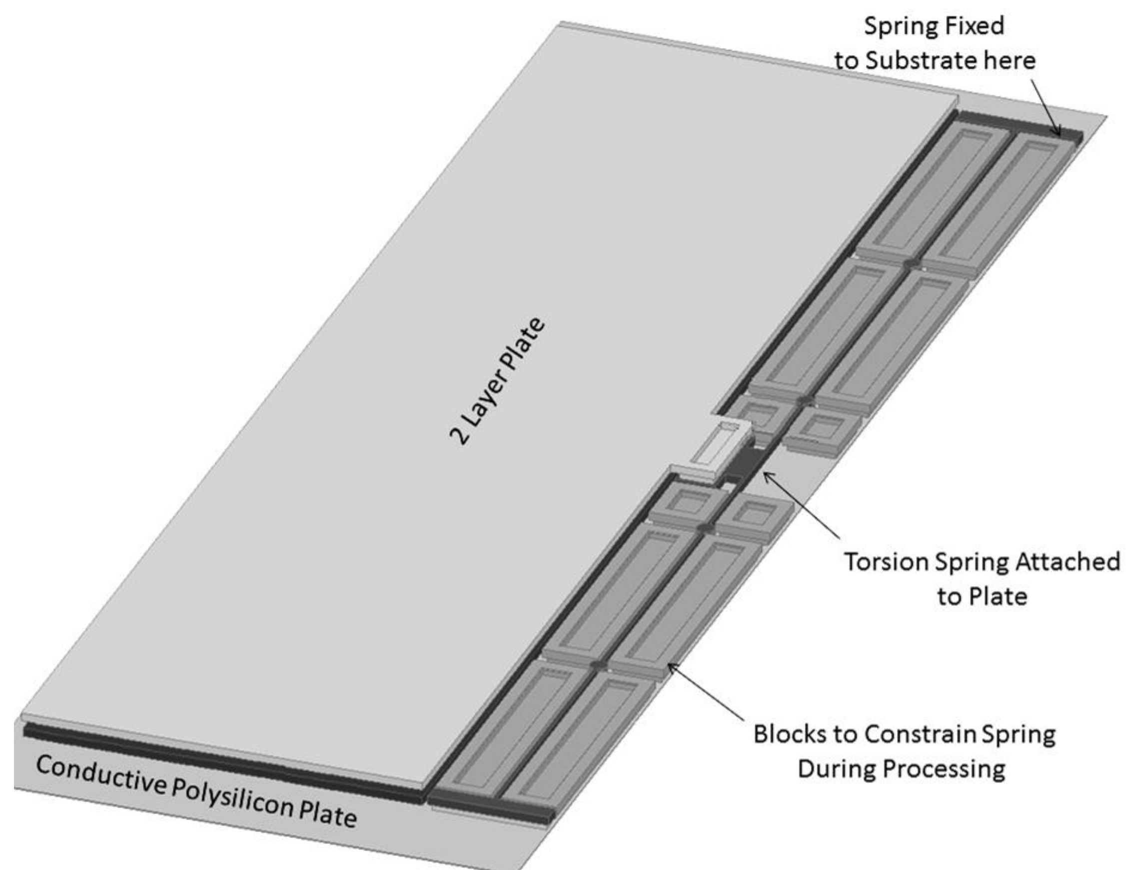

Figure 10. Parallel spring test actuator. The plates are attached to a torsion spring fixed to the substrate. The green constraint blocks protect the spring from excessive motion during processing.

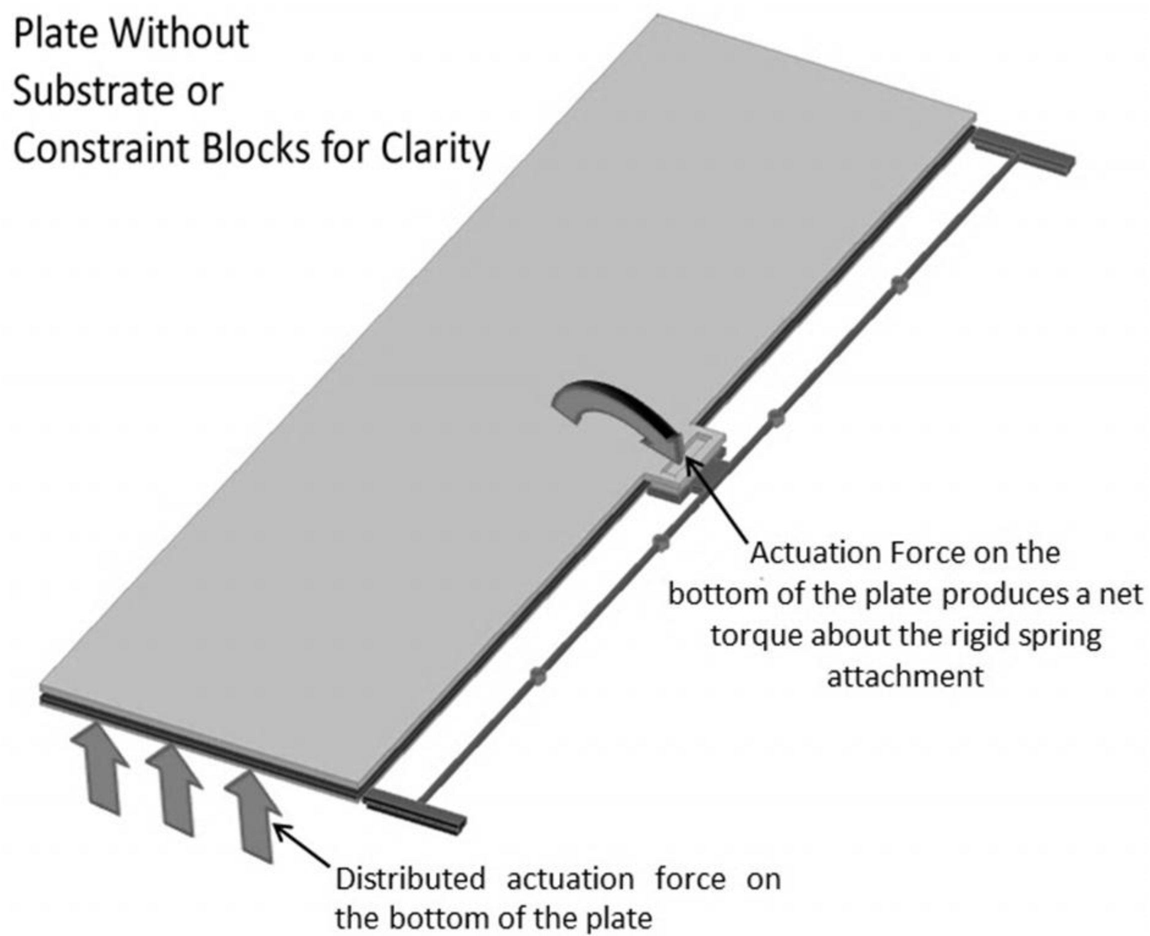

Figure 11. A force lifts the plate to twist a compliant hinge. A continuous, but likely non-uniform, actuation load acts on the bottom of the plate in repulsion against the substrate to twist two torsion springs in parallel.

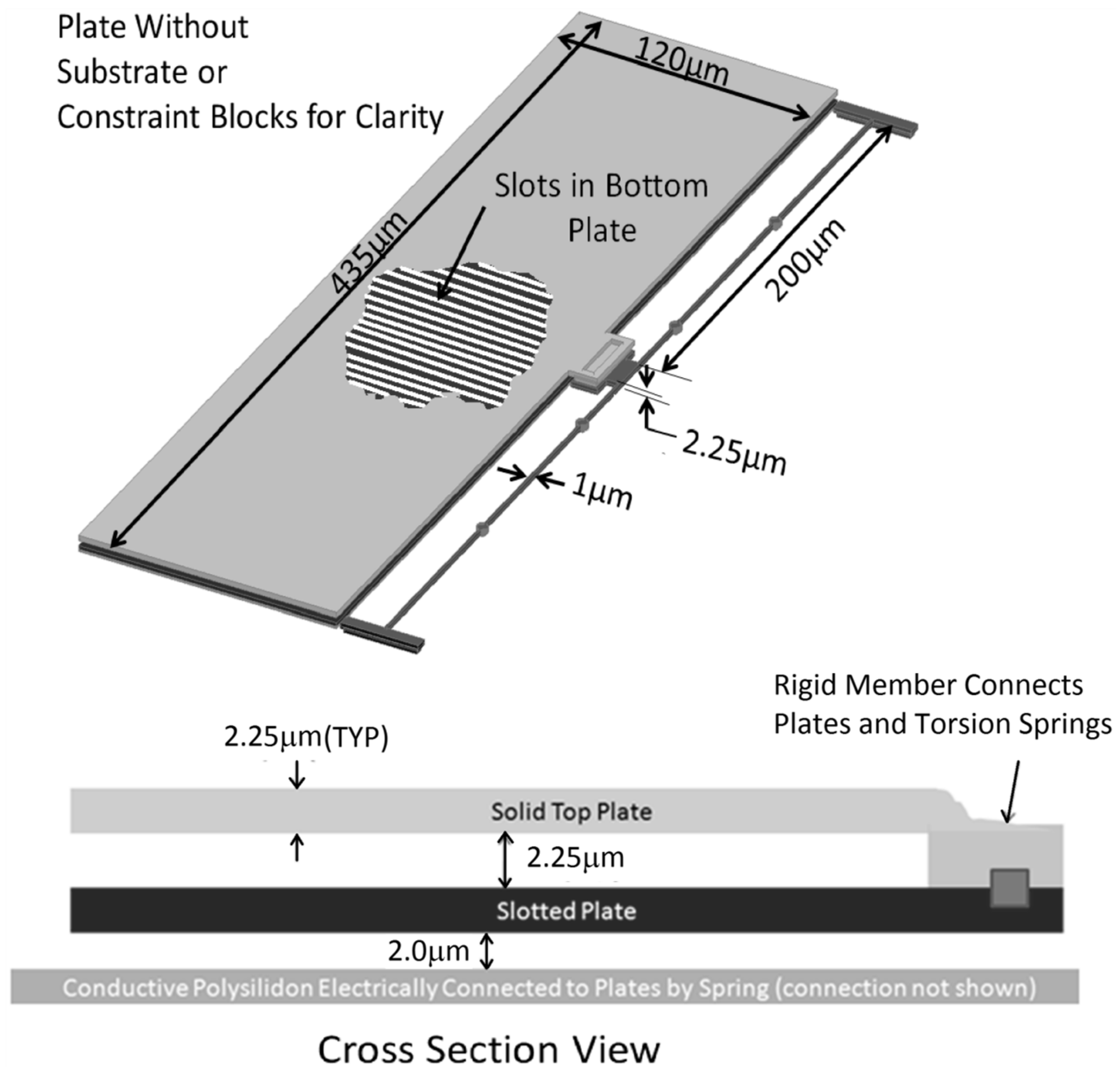

Figure 12. Geometry of a plate actuator with compliant hinge. Dimensions of the spring are shown. Two polysilicon layers 2.25 μm apart constitute the rigid plate. The bottom layer has slots that increase the exposed area and amplify the actuation force by fringing fields.

A linear stiffness of the torsion spring is derived by generalizing the strain energy in terms of the load and applying Castigliano's theorem [20]. Since one length of each cantilever torsion spring is at least eight times longer than any cross-sectional dimension, the total potential energy, *Π*, under the torsion moment, *T,* may be expressed by equation (1).

$$\Pi = \int_0^s \frac{T^2 ds}{2GJ} \tag{1}$$

where *A* is the cross-section area, *I* the area moment of inertia, *E* modulus of elasticity, *G* modulus of rigidity, *s* arc length, and *J* a torsion correction factor [20].

According to Castigliano's theorem, the linear stiffness *K* of one cantilever beam is the derivative of the generalized strain energy with respect to an arbitrary twist θ [20]. Equation (2) shows the calculation in terms of the geometric and material properties of the beam.

$$K = \frac{T}{\theta} = \theta\left(\frac{\partial \Pi}{\partial T}\right)^{-1} = \int_0^s \frac{T^2 ds}{2GJ} = \frac{2\mathrm{T}s}{2GJ} \tag{2}$$

Based on the dimensions shown in Figure 12, and the experimentally obtained torsion constant in Cook [20], the total stiffness is obtained by adding the stiffness of each cantilever spring (equation (2)) in parallel to get the cumulative stiffness in equation (3).

$$K = \frac{0.54\ \mu m^4 G}{200\ \mu m} + \frac{0.54\ \mu m^4 G}{200\ \mu m} = \frac{1.1\ \mu m^4 64\ Gpa}{200\ \mu m} = 344\ \mathrm{p}Nm \tag{3}$$

The plate actuator designed by the author deflects 30° in Figure 13 about the centroid of the torsion beams. The compliant hinge is a force gauge that indicates the plate generates 180 pNm of torque (an equivalent 57 Pa follower pressure on the plate) in Figure 13. Under different beam conditions, the plate also stood out-of-plane at an angle perpendicular to the substrate, which suggests 534 pNm of torque (an equivalent 170 Pa uniform follower pressure on the plate).

The torsion spring shows itself capable of rotating about a single point away from the substrate like a hinge. The parallel cantilever springs move through the 90° motion expected of a bushing hinge.

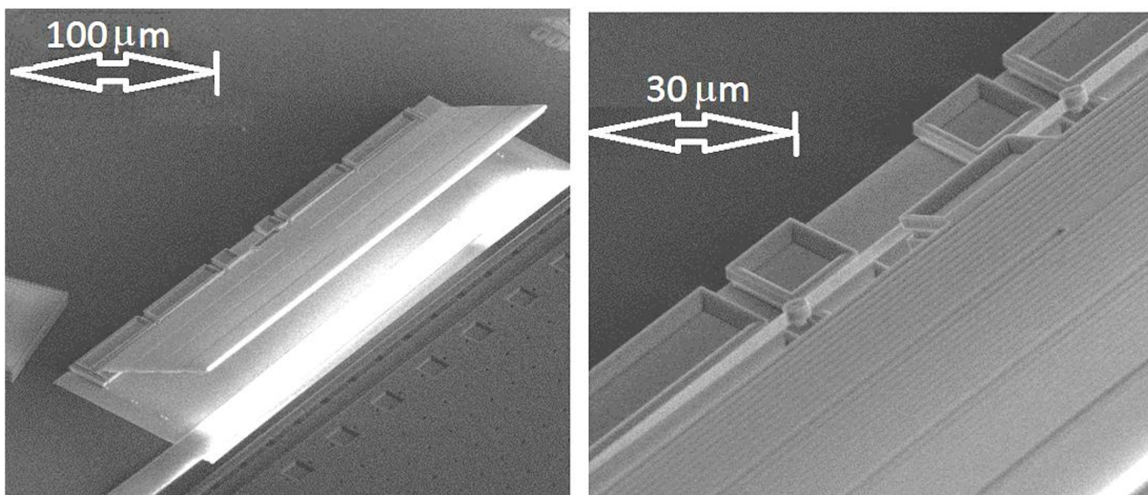

Figure 13. Micrographs of the torsion spring experiment. Compliant hinge connected to a plate coming out-of-plane due to dynamic charge injection, activated in-situ by the scanning electron microscope. The plate deflects 30° out-of-plane from which we deduce 180 pNm available torque. The right image shows a close-up of the hinge twisting about the centroid of the beam [32].

2.2 Torsion Springs in Series

The compliant hinge in Section 2.1 enables hinge-like motion, but requires a long spring. In cases where torque is low, the spring constant can be reduced by loading several torsion springs in series rather than increasing the length of the beam. An experiment that consists of two rigid, parallel rails connected to eight torsion springs in series shows that a compliant series hinge deflects out-of-plane under a torque smaller than 100 pNm with a maximum dimension less than 200 μm. Figure 14 shows the experimental apparatus that uses dynamic charge injection to repel the slider rails from the substrate. The apparatus is attached to a large plate with hinges to compare the stiffness of the spring to the stiffness of the plate.

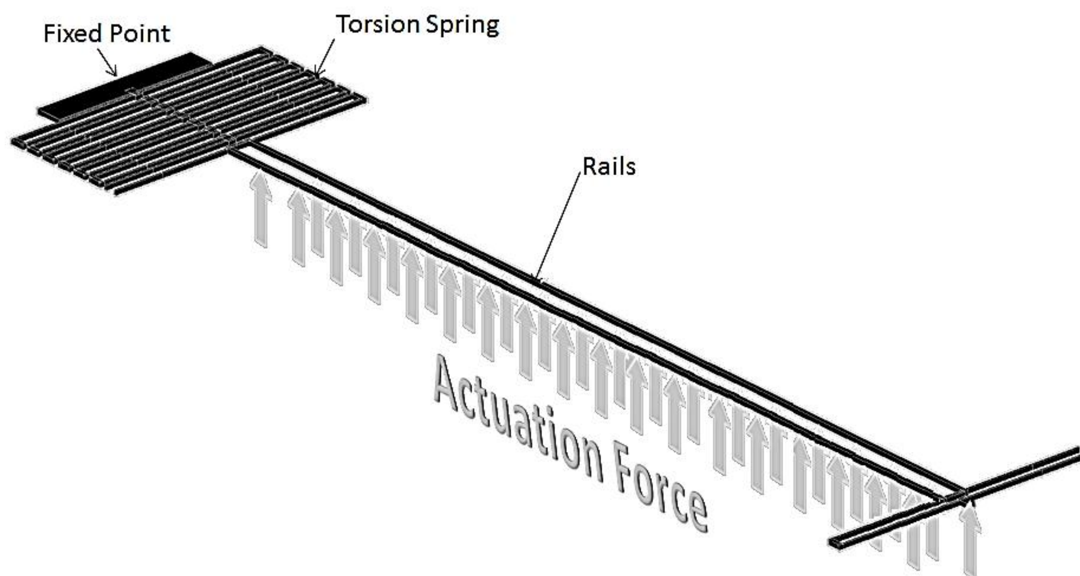

Figure 14 Drawing of series spring connected to rigid rails [33]. Designing around the force only produced by the rail underestimates the actuation force, since the rails have little surface area to generate field lines, and the electrical force on the spring (not shown) will actually be significant.

To model the force/deflection relationship of the spring, we calculate the stiffness of a single beam and then add that stiffness in series and parallel configurations to get the final value. Figure 15 gives the dimensions of the single torsion beam used in the design. The torsion stiffness from equation (2) is modified to account for the geometry in Figure 15, yielding the stiffness in equation (4).

$$K = \frac{0.54\ \mu m^4\ 64\ Gpa}{63\ \mu m} \tag{4}$$

To increase stability, two of the springs are loaded in parallel, as shown in Figure 16.

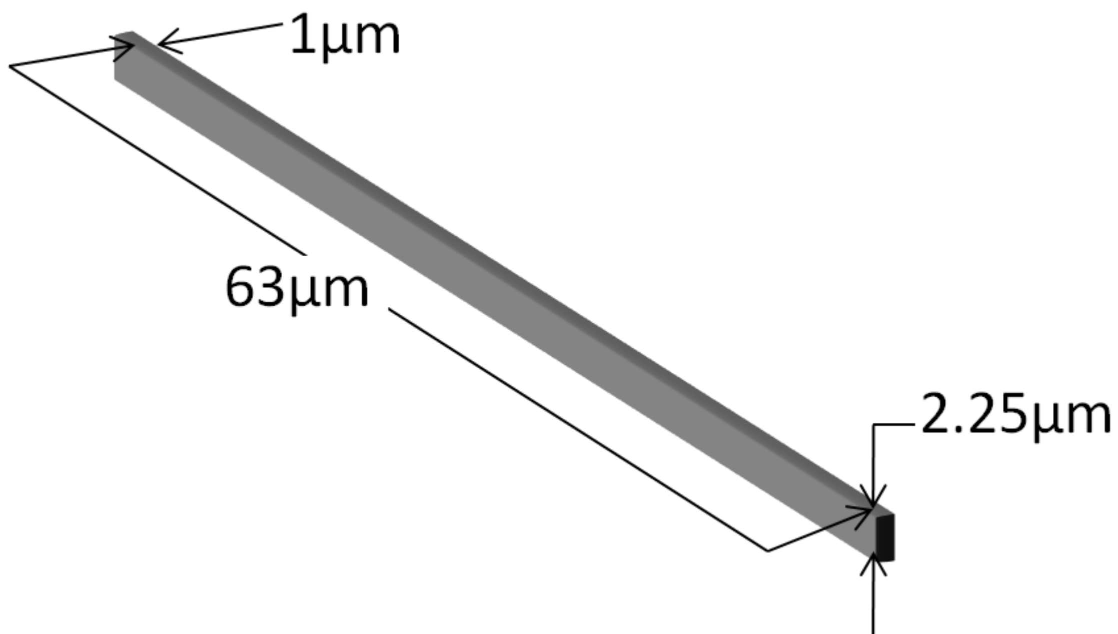

Figure 15. Dimensions of a single beam used in the torsion springs shown in Figure 14.

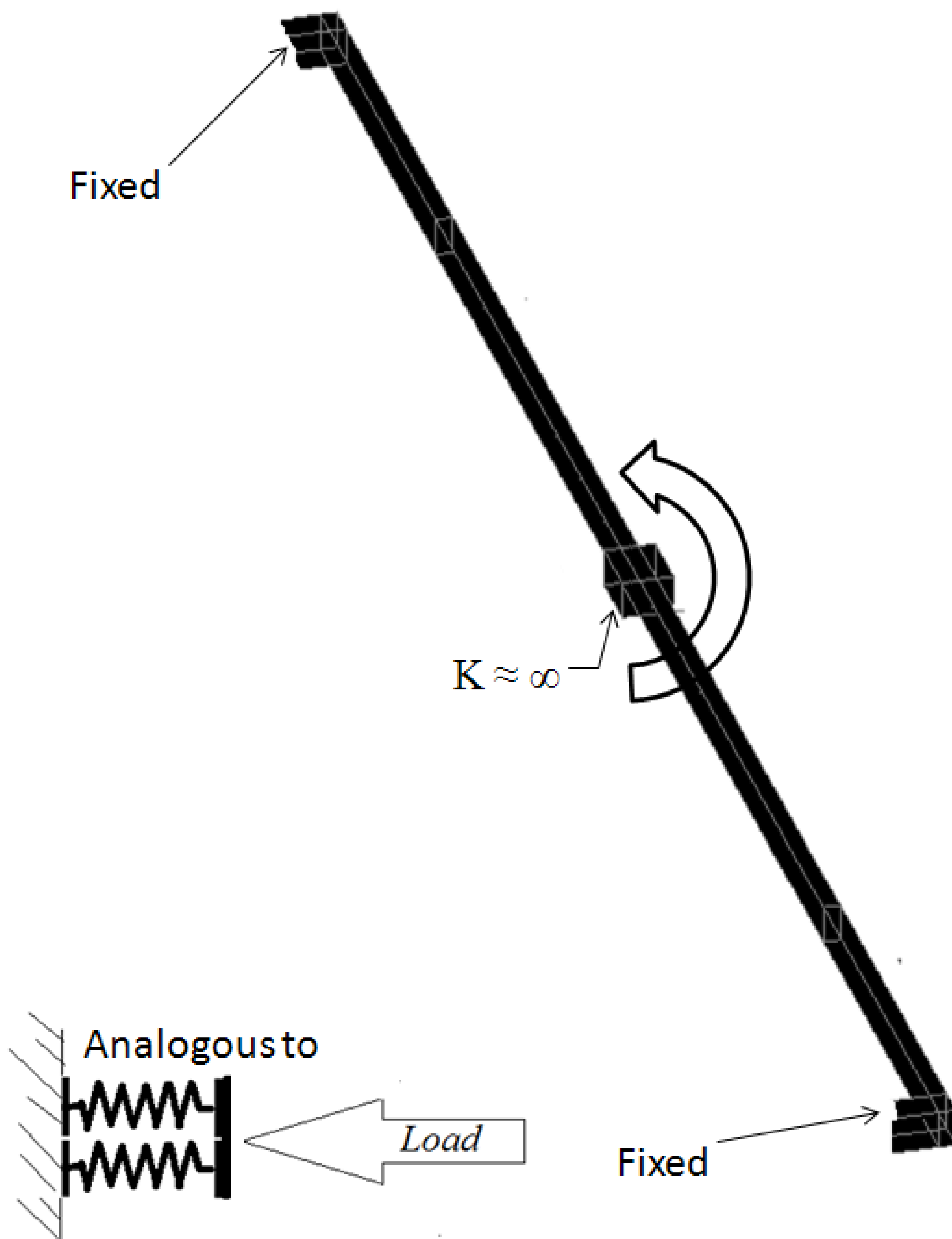

Figure 16. Torsion spring in Figure 15, loaded in parallel by a rigid block.

The parallel load doubles the stiffness in equation (4) to that of equation (5).

$$K = \frac{0.54\ \mu m^4\ 64\ Gpa}{63\ \mu m} + \frac{0.54\ \mu m^4\ 64\ Gpa}{63\ \mu m} = 2\frac{0.54\ \mu m^4\ 64\ Gpa}{63\ \mu m} \quad (5)$$

Joining two of the parallel springs in series (Figure 17) reduces the spring constant in equation (5) to the original value from equation (4) as shown in equation (6).

$$K = \left(\left(\frac{1}{2}\right)\frac{63\ \mu m}{0.54\ \mu m^4\ 64\ Gpa} + \left(\frac{1}{2}\right)\frac{63\ \mu m}{0.54\ \mu m^4\ 64\ Gpa}\right)^{-1} = \frac{0.54\ \mu m^4\ 64\ Gpa}{63\ \mu m} \quad (6)$$

Finally, to reduce the stiffness in equation (6), six of the springs from Figure 17 and two of the springs from Figure 15 are loaded in series. The final stiffness is calculated in equation (7) by adding the stiffness in equation (6) as eight torsion spring in series as shown in Figure 18. The stiffness of every spring is the same and the cumulative stiffness is found with a factor of eight.

$$\mathrm{K} = \left((8)\frac{63\ \mathrm{\mu m}}{0.54\ \mathrm{\mu m}^4\ 64\ \mathrm{Gpa}}\right)^{-1} = 68\ \mathrm{pNm} \quad (7)$$

The torsion spring connects the slide rails to a rigid plate attached to a conductive shell over the substrate by mechanical hinges. The bottom plate uses three mechanical hinges. In Figure 19, the spring bends more than 35° out-of-plane, suggesting that it experiences a 42 pNm torque. Series torsion springs thus enable out-of-plane deflection similar to a mechanical hinge.

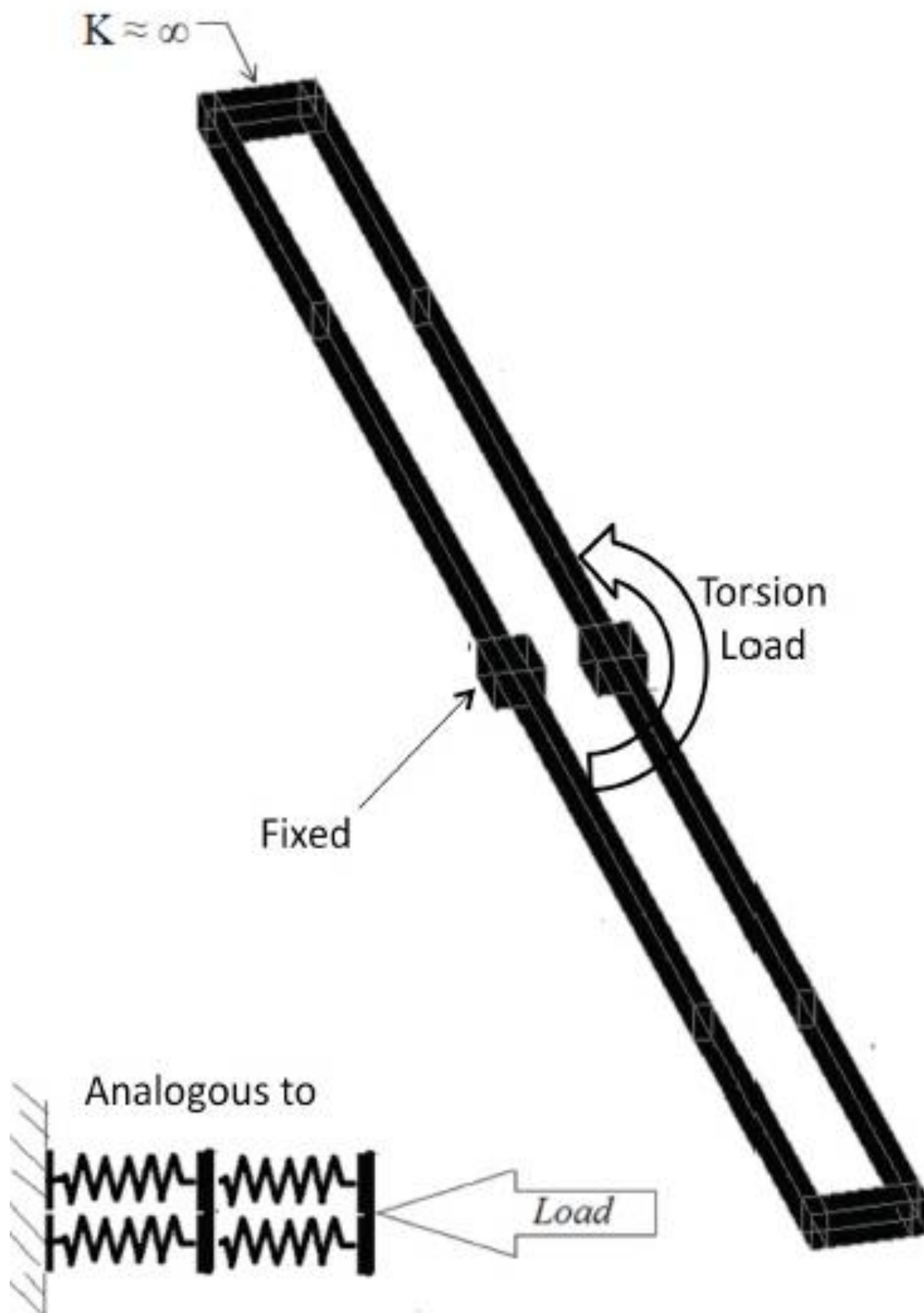

Figure 17. Two parallel beams in series. Two sets of parallel torsion springs joined in series by rigid members on either end.

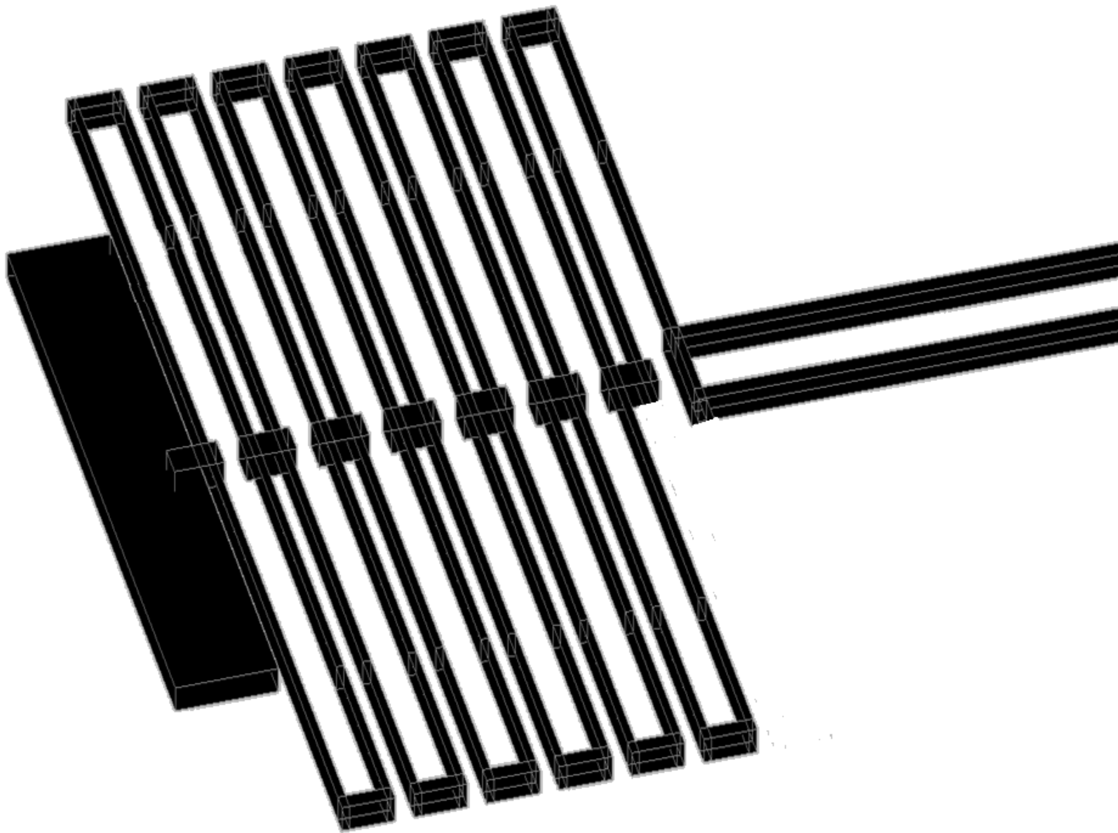

Figure 18. Entire torsion spring for the experiment from Figure 14 [33]. The final device is built from layer 3 of the SUMMiT-V^{TM} process. Because of a CAD placement error, the last spring is incomplete.

The experiment in Figure 19 shows that the torsion spring is more compliant than the bushing hinges. The plate experiences a load generated from its own geometry plus the load from the two rails yet it only deflects 8° out-of-plane. Meanwhile, the slider rail portion, which only experiences the load generated by its own geometry, is able to deflect four times as much as the hinges. The disparity between the compliant portion and hinged portion indicates that the three bushing hinges are less able to move out-of-plane than the torsion spring.

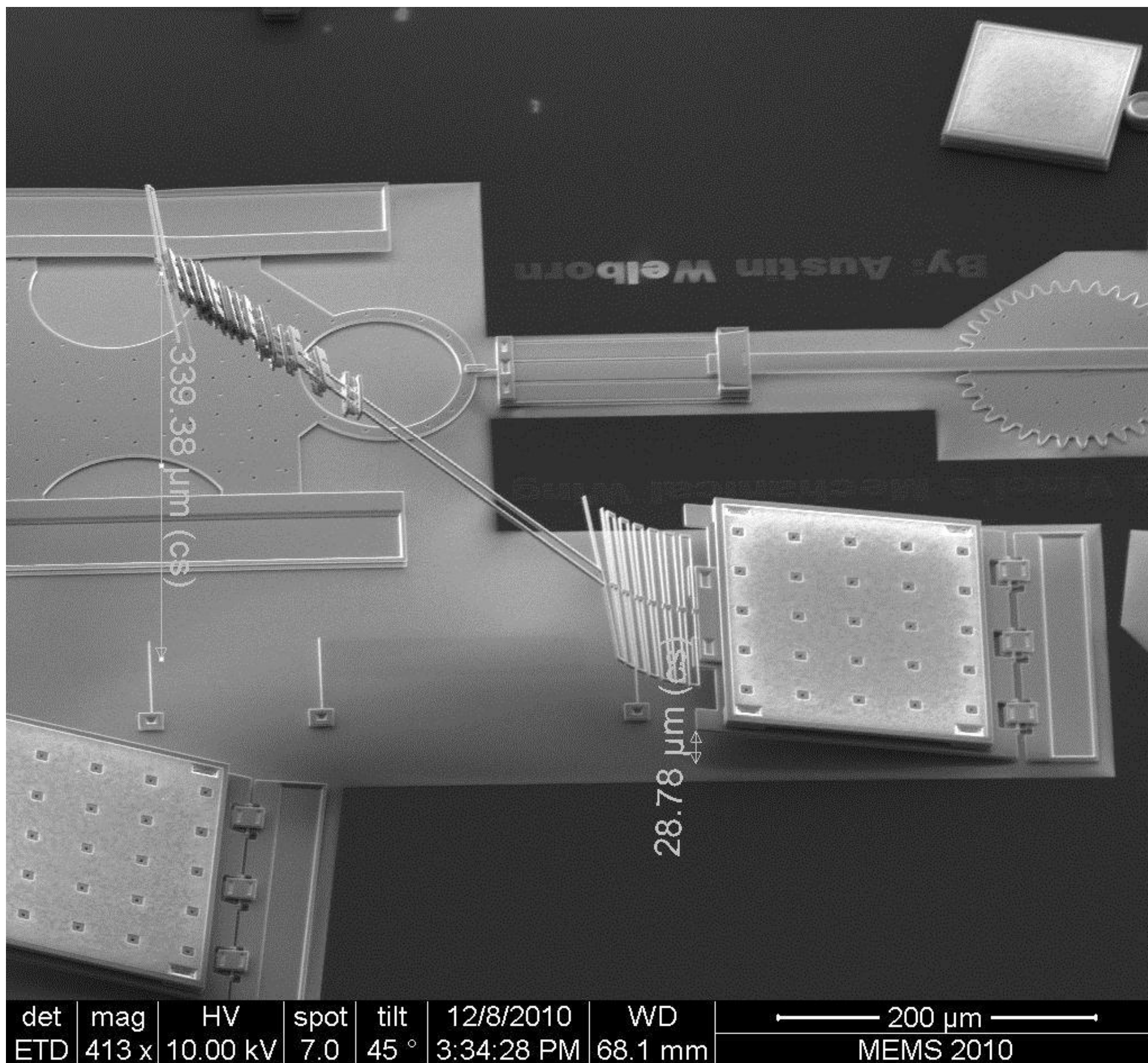

Figure 19. Torsion springs in series allow rigid beams to move out-of-plane [33]. The track on the compliant hinge stands further out-of-plane than the plate. The mechanical hinges offer more resistance than the compliant hinge.

CHAPTER 3

CASE-STUDY– TORSION BISTABLE MECHANISM

3.1 Background to Microcompliant Bistable Mechanisms

The bushing-style MEMS hinge is commonly used to construct permanent out-of-plane structures. A compliant hinge with elastic locking capabilities would improve upon existing techniques [33,34] by eliminating the use of hinges.

Until now, only South Carolina University reported a nonbuckled micro-compliant bistable mechanism that acts out-of-plane. South Carolina University's device directed the in-plane motion of a compliant linkage out-of-plane with a spherical linkage [33]. Though South Carolina's experiment did achieve out-of-plane motion with an elastic bistable device, it did not use an out-of-plane torque, and the spherical linkage uses bushing hinges to achieve the desired motion. The microcompliant mechanism presented here deforms under a simple out-of-plane torque similar to a hinge. Our compliant mechanism is a micropolysilicon hoop that achieves a second stable state by being turned inside-out. A model using finite element analysis is used to assess the stability and stiffness of the micro-elastic hoop.

3.2 Modeling a Micro-Elastic Ring

A finite element beam model is used to characterize the stiffness of the polysilicon ring. The finite element model uses 100 straight Timoshenko beam elements that account for cross-section warping (ANSYS *Beam188*) [36]. The model assumes opposing concentrated torsions on the ends of the polysilicon hoop in Figure 20.

The quasi-static solution diverges, and is approximated by adding a dynamic relaxation term [37]. The quasi-static model with dynamic relaxation converges when the damping constant is .0005. Appendix A contains a copy of the ANSYS code and Figure 21 the force deflection code generated by it. The maximum torque[3] is 30 pNm and the maximum engineering shear stress is 600 MPa.

The model was not definitively validated with an experimental force/deflection curve. Instead, experiments were performed to locate the second stable point and demonstrate that the elastic hoop is indeed bistable.

The test structure in Figure 22 uses two large plates connected to the elastic ring. A probe tip pushes the plates toward the center and twists the polysilicon hoop inward. Ten straps laterally constrain the elastic hoop to ensure that the twisting moment translates to a concentrated torsion. (The constraint straps also introduce frictional contact).

---

[3] The linear curved beam torsion formulas in [20] conservatively predict a torque of 36 pNm to twist a fixed quarter arc cantilever beam 180°, with the same curvature and cross-section dimensions as in Figure 20 [39].

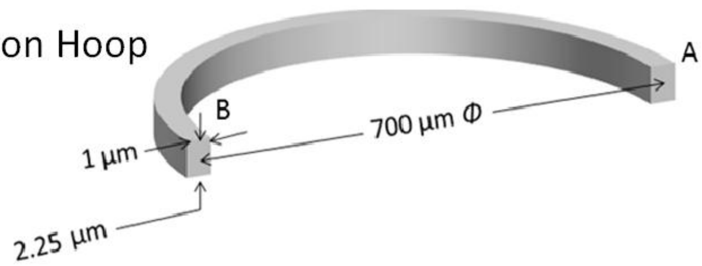

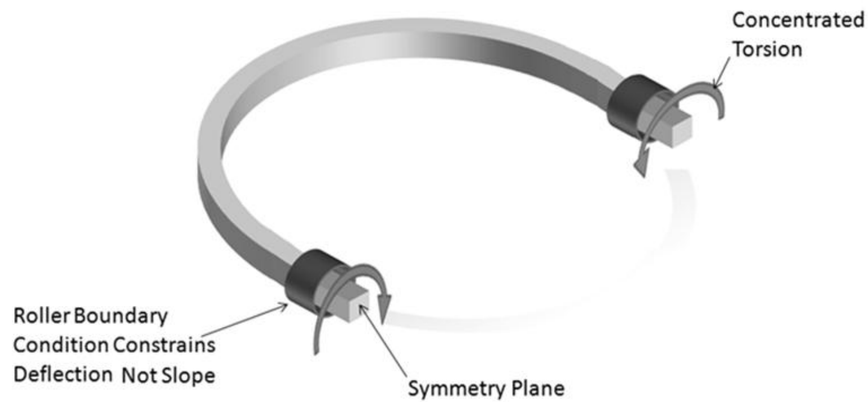

Figure 20. Boundary conditions applied to an elastic hoop beam model. The total Lagrangian beam mesh of the compliant elastic hoop has concentrated moments applied to a symmetric mesh constrained by rollers at the end nodes.

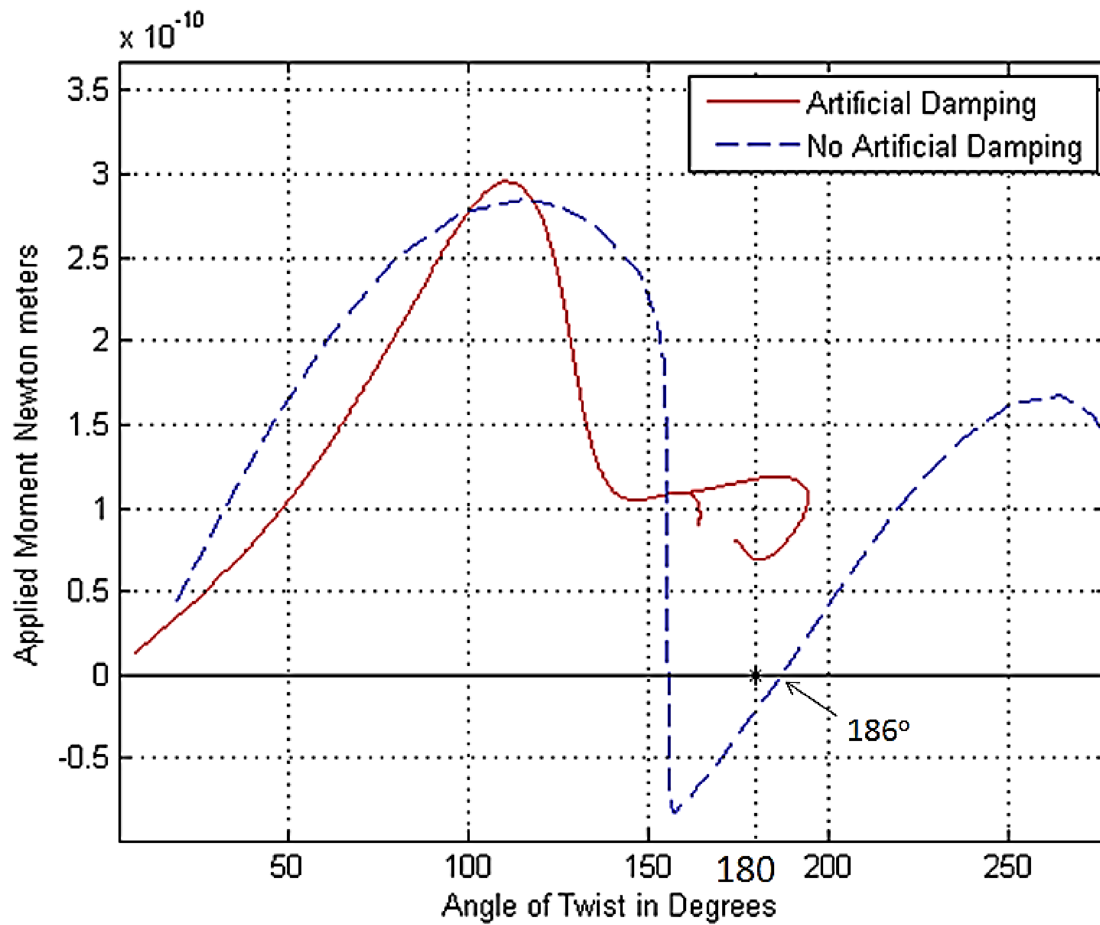

Figure 21. Response of the micro-elastic hoop with and without artificial damping. The quasi-static force/deflection curve does not converge unless it includes artificial damping. The artificial damping reduces the accuracy of the solution but models the entire force/deflection curve and identifies the second stable position as occurring at 186°.

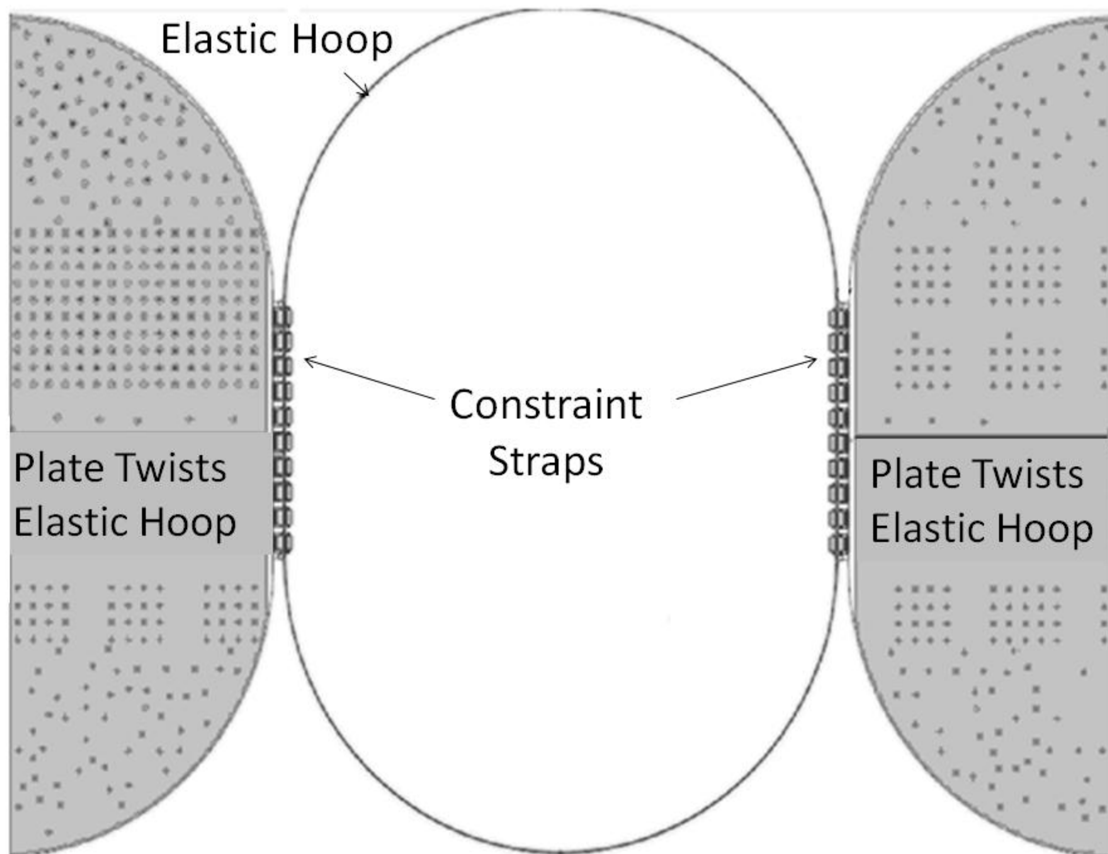

Figure 22. Architecture of the elastic ring test structure. Ten constraint straps maintain adjustment, keep the device from floating during etch processes, and concentrates the torsion of the plates about the centroid.

A manual load was applied to the test structure to locate the stability points. In Figure 23, frame 7, the plate touches the center of the hoop. At this point, the elastic hoop is twisted 180° and has not yet pulled into its second stable position. The behavior is consistent with the stability predicted by the model.

To flip the ring into its second stable state, the second stable point is brought to 180° by changing the curvature of the hoop. Experience with elastic hoops has shown that reducing the curvature perpendicular to the loading points moves the snap through region closer to the axis-symmetric snap through region (90°-180°) [39]. The elastic hoop was

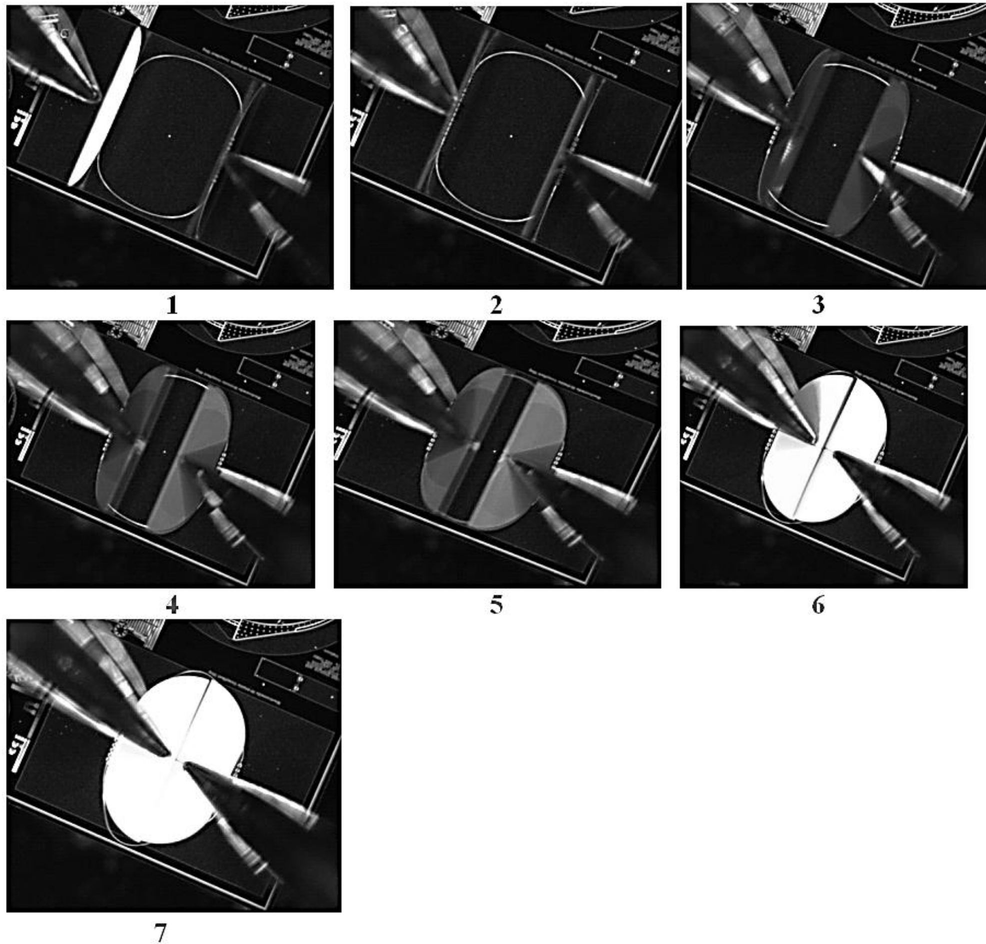

Figure 23. Probe tips hold the plates down in a manually actuated experiment. The plates spring upward if the probe tip is removed, indicating that the elastic hoop is not in a stable configuration [38].

broken from the substrate and then pulled outward, as shown in Figure 24, to flatten the curvature.

In Figure 25 the ring is broken off of the substrate and stretched outward to snap the spring into its second stable position.

Figure 26 shows the ring sitting in its second stable position without an outside force. This experiment proves that a micro-elastic hoop is bistable, and the model accurately predicts stable configurations.

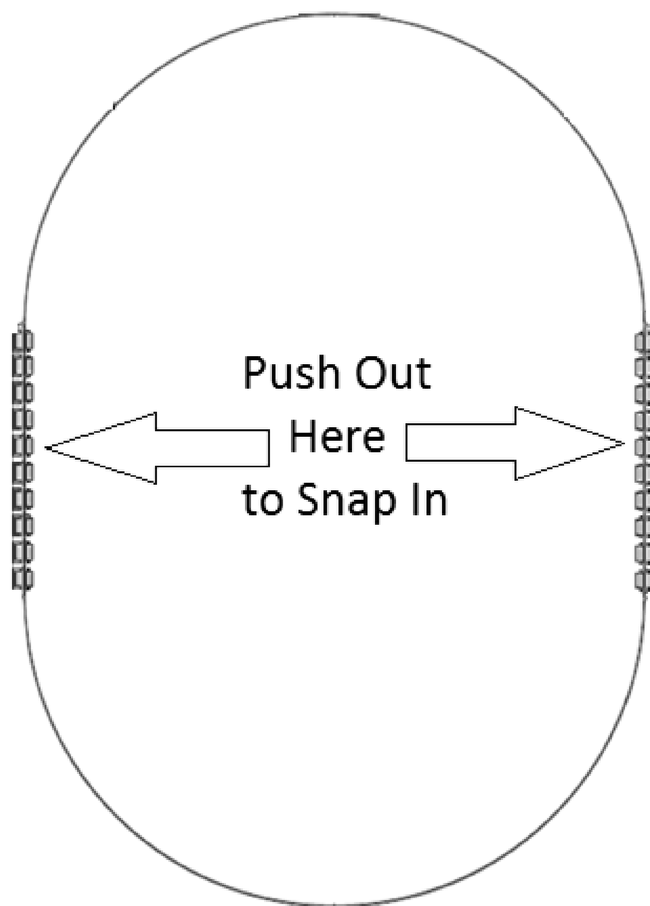

Figure 24. How to flatten the curvature of the spring. The flatten curvature changes the snap through point so that the twist imparted in Figure 23 attains a bistability point of 180° and turns it inside-out.

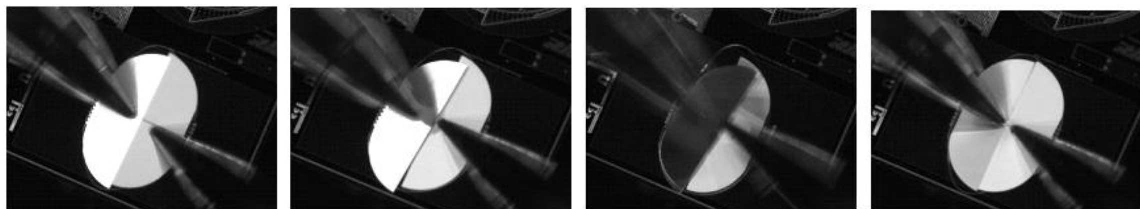

Figure 25. A spring pulled off of its hinges and forced into the second stable state. The hoop is pulled off of the substrate to flatten the curvature. The flattened curvature changes the snap through point of the ring and it snaps into a second stable position [38].

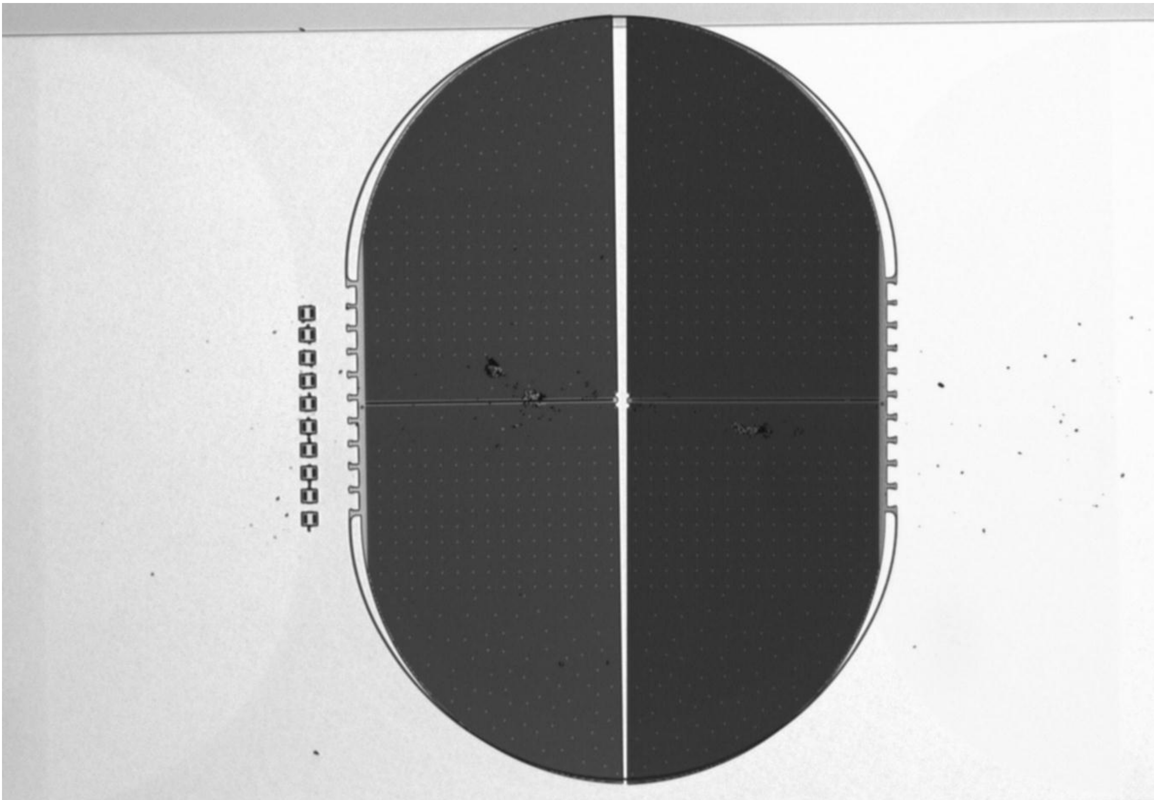

Figure 26. Photograph of the micro-elastic hoop in a second stable position.

In conclusion, it is evident that an elastic hoop compliant mechanism is a feasible bistable compliant hinge replacement. Though the force/deflection curve is not validated, the experiment suggests that the second stable state happens after 180° as the model predicts. In the future, the as-manufactured curvature could be designed such that the hoop snaps into the second stable state before it is twisted 180°. The elastic hoop mechanism shows promise as a compliant elastic threshold hinge.

CHAPTER 4

CASE STUDY– RADIAL MOTION TRANSDUCER

In-plane compliant linkages do not have to use rigid links with compliant pin joints. They can rather center on a simple flexible member or series of flexible members that naturally deflect through the stroke of the linkage. We have designed a compliant version of the complex Hoberman linkage system from Figure 7 that demonstrates this concept. The compliant rotational force transducer in Figure 27 eliminates the slider and pin joint linkages with curved beams fixed to a ring gear.

The compliant arcs are laid out so that they cross the ring gear at their perpendicular bisection. The perpendicular constraint encourages the tangential load to act parallel to the cross-section and limits buckling[4]. The other fixed end of the arc does not move with the ring gear. Figure 28 shows how the torque on a ring gear squeezes the compliant arc by moving the guided tip toward the fixed end. The resultant compression moves the crest of the arc outward and produces radial motion.

---

[4] Simulations of different loading conditions showed that when a component of the load acts normal to the cross-section, the arc becomes more susceptible to out-of-plane buckling. The fixed condition at either end of the compliant arc, however, also reduces the danger of buckling. The arc does not necessarily need to connect at the perpendicular bisection.

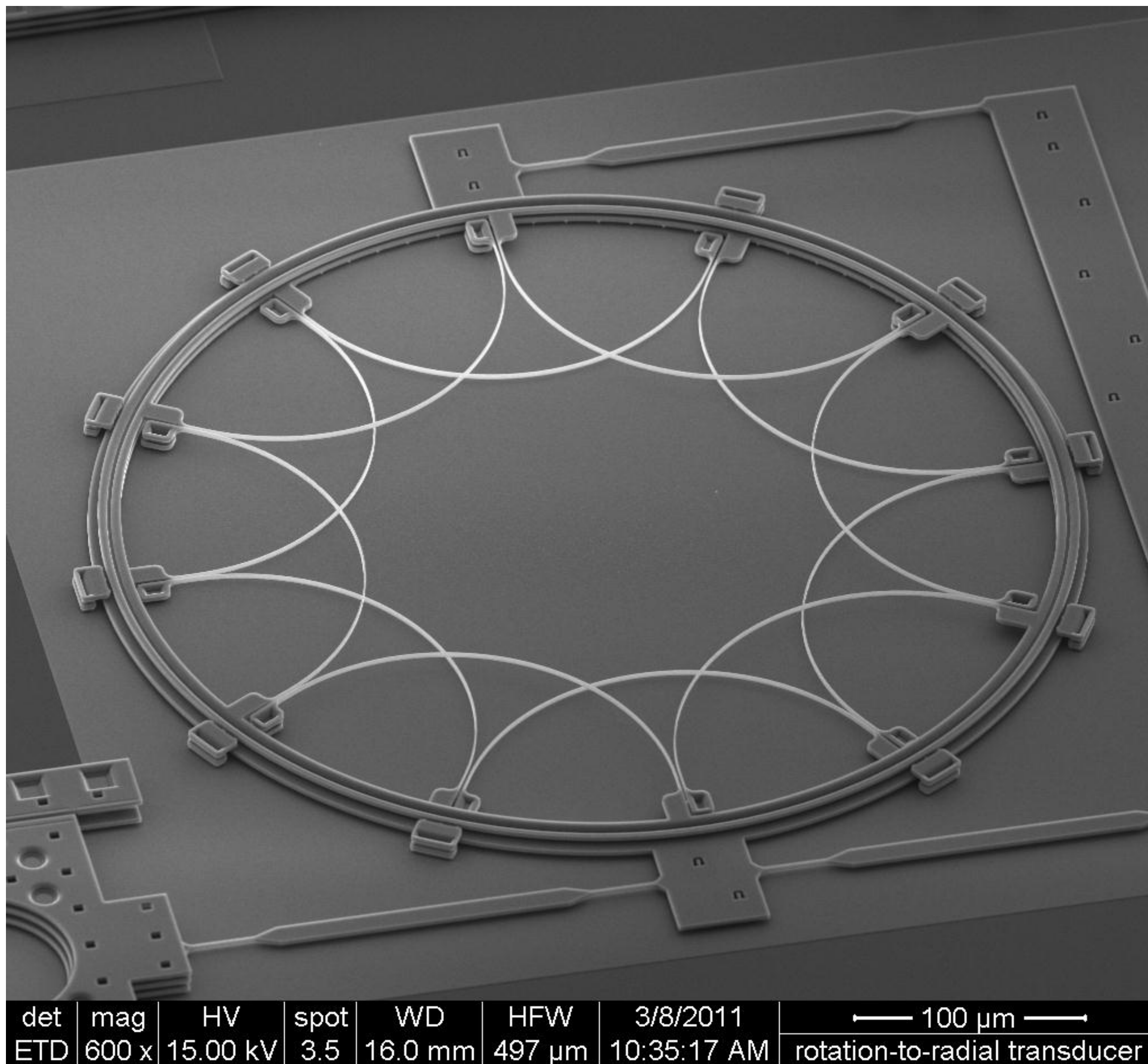

Figure 27. Compliant rotation-to-radial motion transducer.

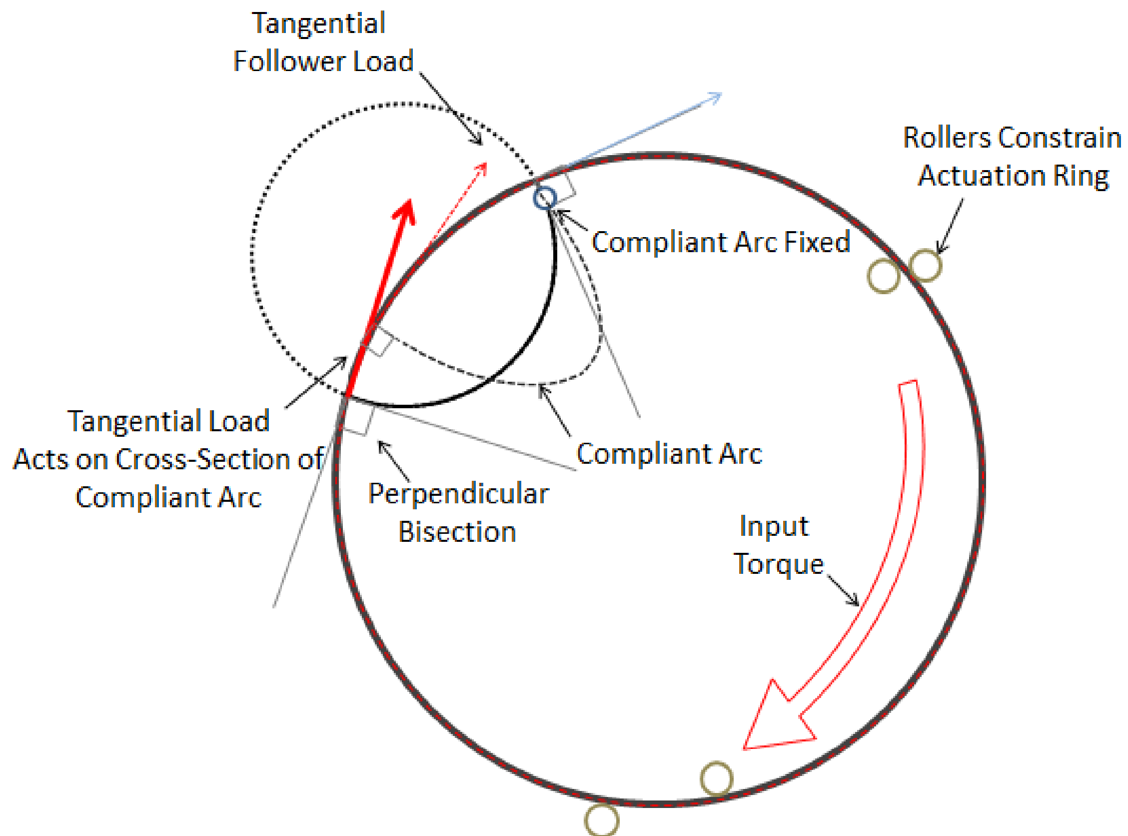

Figure 28. Basis for the compliant rotation-to-radial motion transducer. A ring that is free to turn about its center has a compliant arc attached to it and the substrate, so that when the ring twists, it squeezes the arc.

The beam elements[5] in Frank Pai's geometrically exact structural analysis code (GESA) that accompanies his book [23] is used to model the compliant arc. The exact motion of the arc shown in Figure 28 cannot be modeled because GESA does not facilitate position control. The boundary condition is approximated by assuming the point fixed to the ring moves in a straight line (Figure 29).

The main file to run this simulation in GESA is provided in Appendix B. The file includes MATLAB code to generate the mesh and orient it so that the assumed deflection aligns with the horizontal axis of the global coordinates in GESA.

The nonlinear curved beam model demonstrates that a compliant arc translates a horizontal deflection in the vertical direction. The displacement is limited in the radial direction. After a 11 μm input, the resultant radial translation diminishes. The horizontal to vertical motion can be approximated by two linear ratios. Before 11 μm, the radial motion is about .64 μm/μm that of the tangential motion. After 11 μm, the ratio decreases to .02 μm/μm. The translation ratio decreases by approximately 95%. Figure 30 compares the assumed linear translation ratio to the actual ratio predicted with GESA.

The drastic reduction in motion displacement ratio corresponds to an increases in the slope of applied tangential load versus the tangential displacement (Figure 31). The load increase at 11 μm corresponds to a 1 Gpa maximum shear stress at the fixed end of the beam.

---

[5] The beam element assumes a deformation consistent with Timoshenko beam theory that uses shear correction factors to account for torsion and shear warping stiffness reduction.

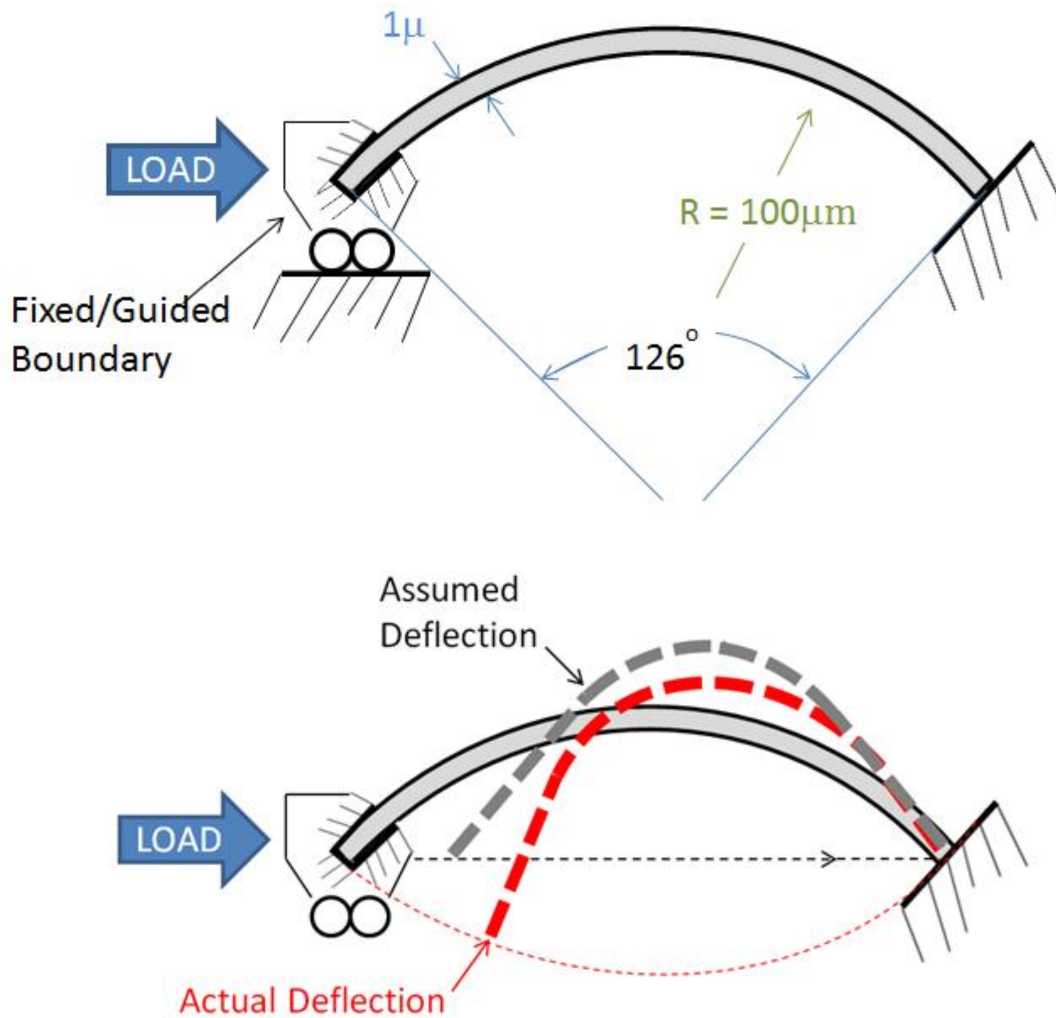

Figure 29. Actual deflection of a compliant arc as compared to the assumed deflection. The actual deflection will follow the curvature of the ring gear. The assumed deflection follows a straight line because GESA does not facilitate displacement control. The assumption neglects the inward motion of the fixed/guided end.

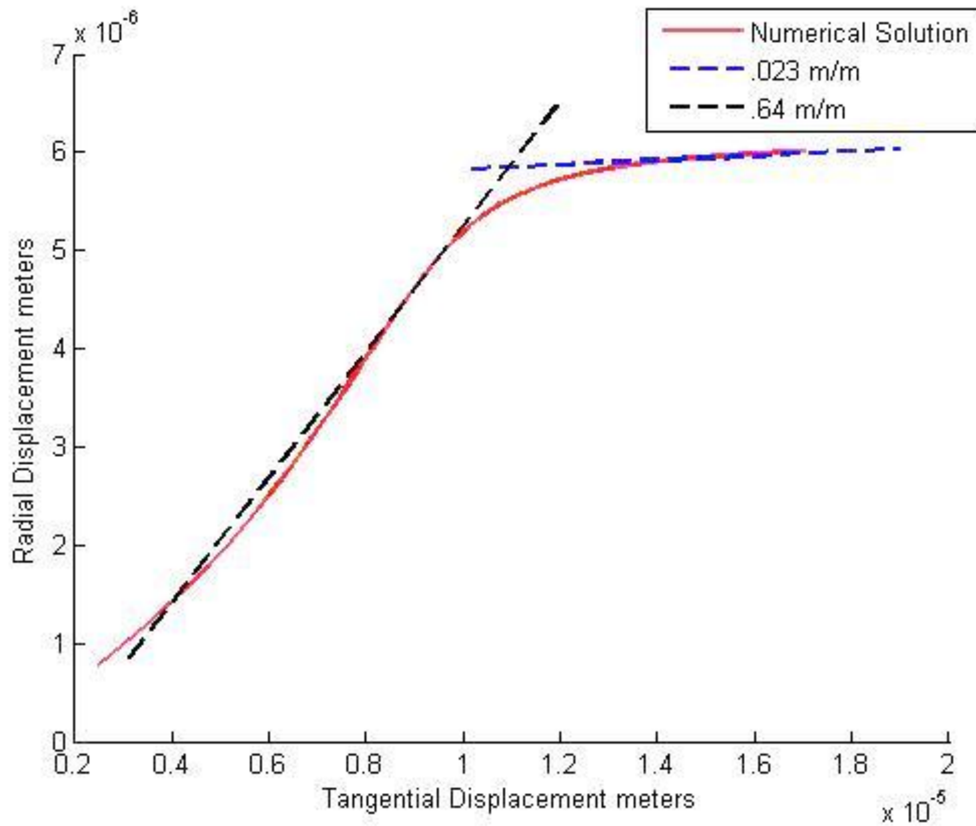

Figure 30. Numerical solution of translation ratio compared to linear ratios. The translation ratio is the radial (or crest of arc in Figure 29) displacement compared to tangential displacement (horizontal displacement in Figure 29). The approximate linear translation ratios intersect when the tangential displacement is 11 μm.

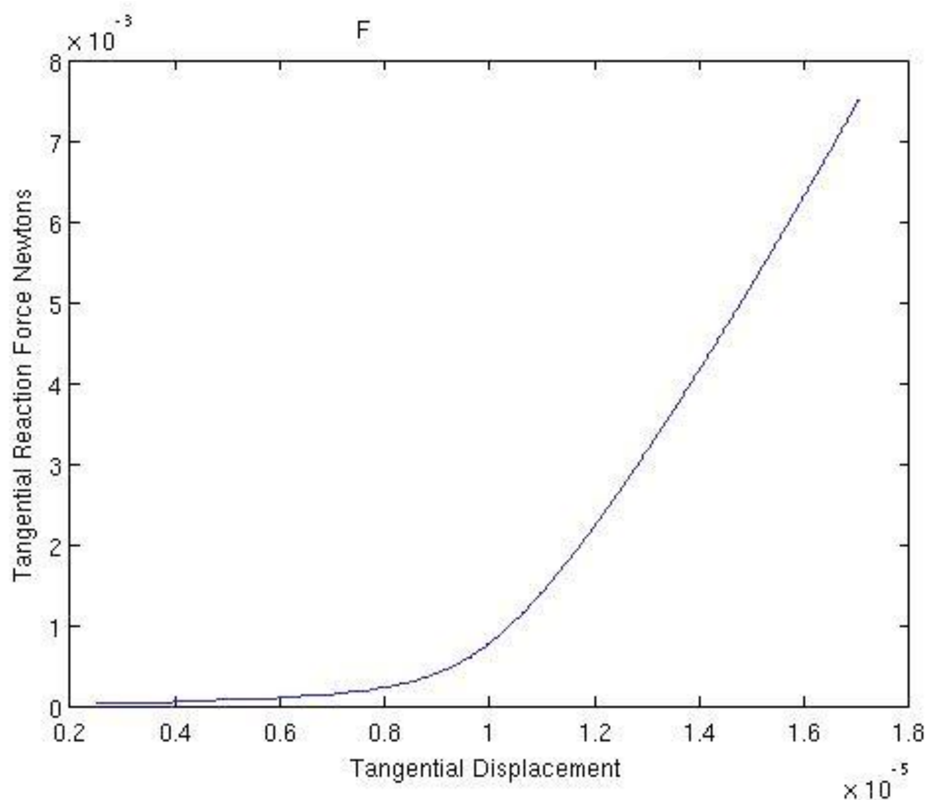

Figure 31. Force/deflection curve of the curved beam in Figure 29.

In Figure 32, six compliant arcs, separated by a one micron gap, attach to a ring gear. Before actuation, the crest of each arc touches the edge of an imaginary 200 μm diameter circle centered inside the ring gear. The transducer does not function in reverse.

In Figure 33 and Figure 34, a stack of two radial ring mechanisms from Figure 32 maximize the number of radial pulling points. The device is not attached to a micro-actuator. Figure 31 indicates that the compliant mechanism requires 10-50 mN to deflect 10-15 μm. No known actuator that would fit within the space constraints of the chip could produce the necessary force and stroke. A manual probe tip slider is instead positioned to actuate the ring and test the mechanism. The experiment in Figure 35 applies a torque that corresponds to more than 16 μm of radial displacement.

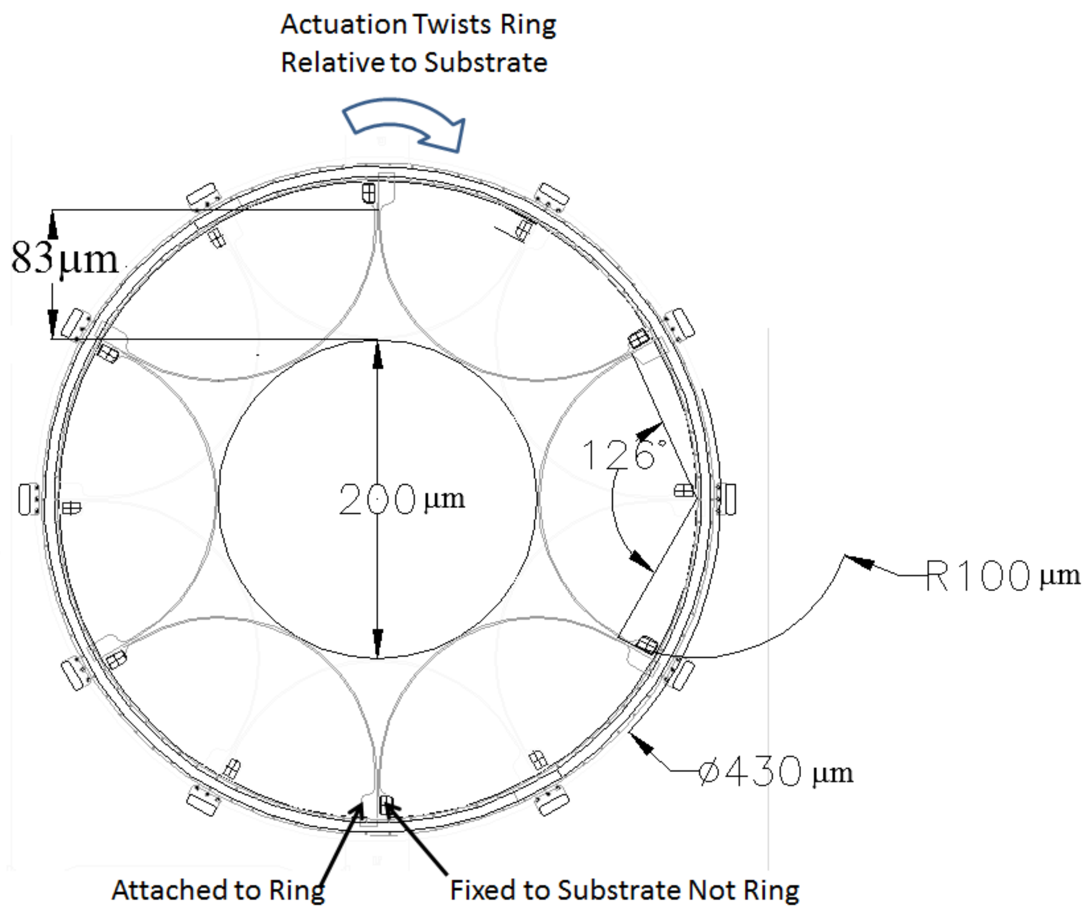

Figure 32. Six compliant arcs attached to a ring in the as-built position. One end of each arc is fixed to the substrate so that when the outer ring rotates, the crests of each arc moves toward the center.

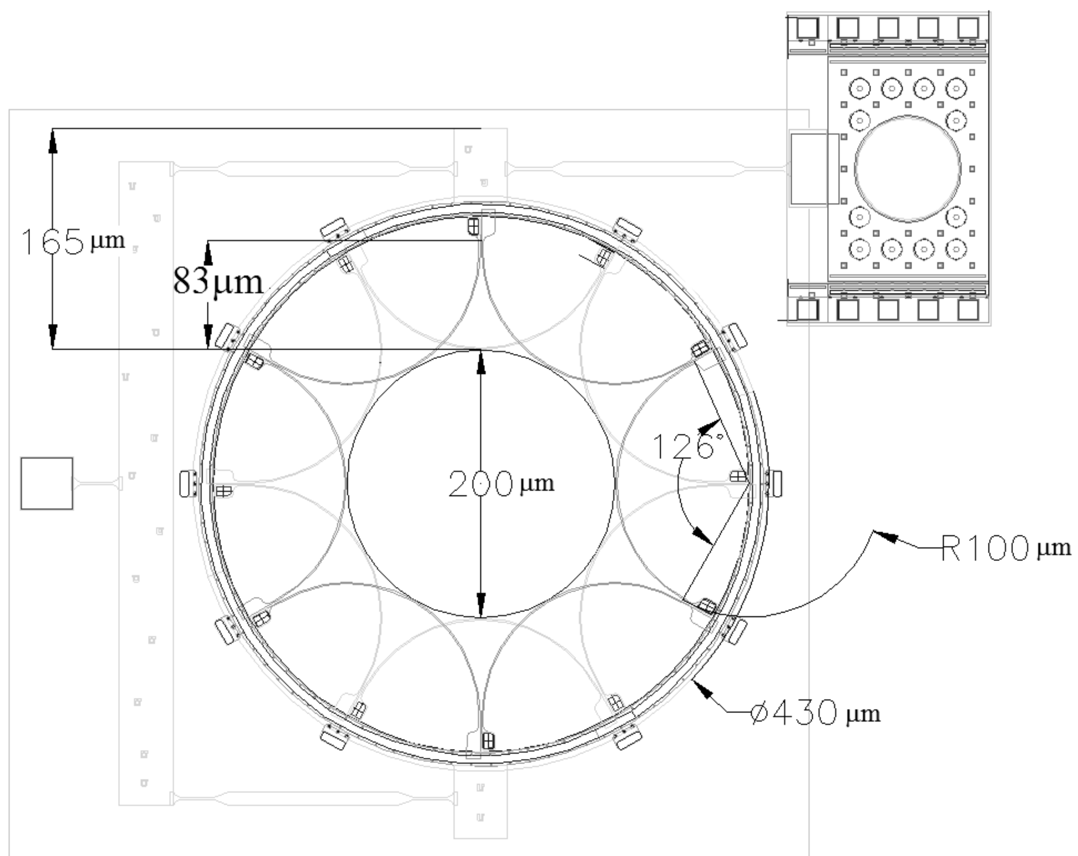

Figure 33. Two-layer compliant motion transducer. Two motion transducers stacked in two layers to increase actuation points on the center circle.

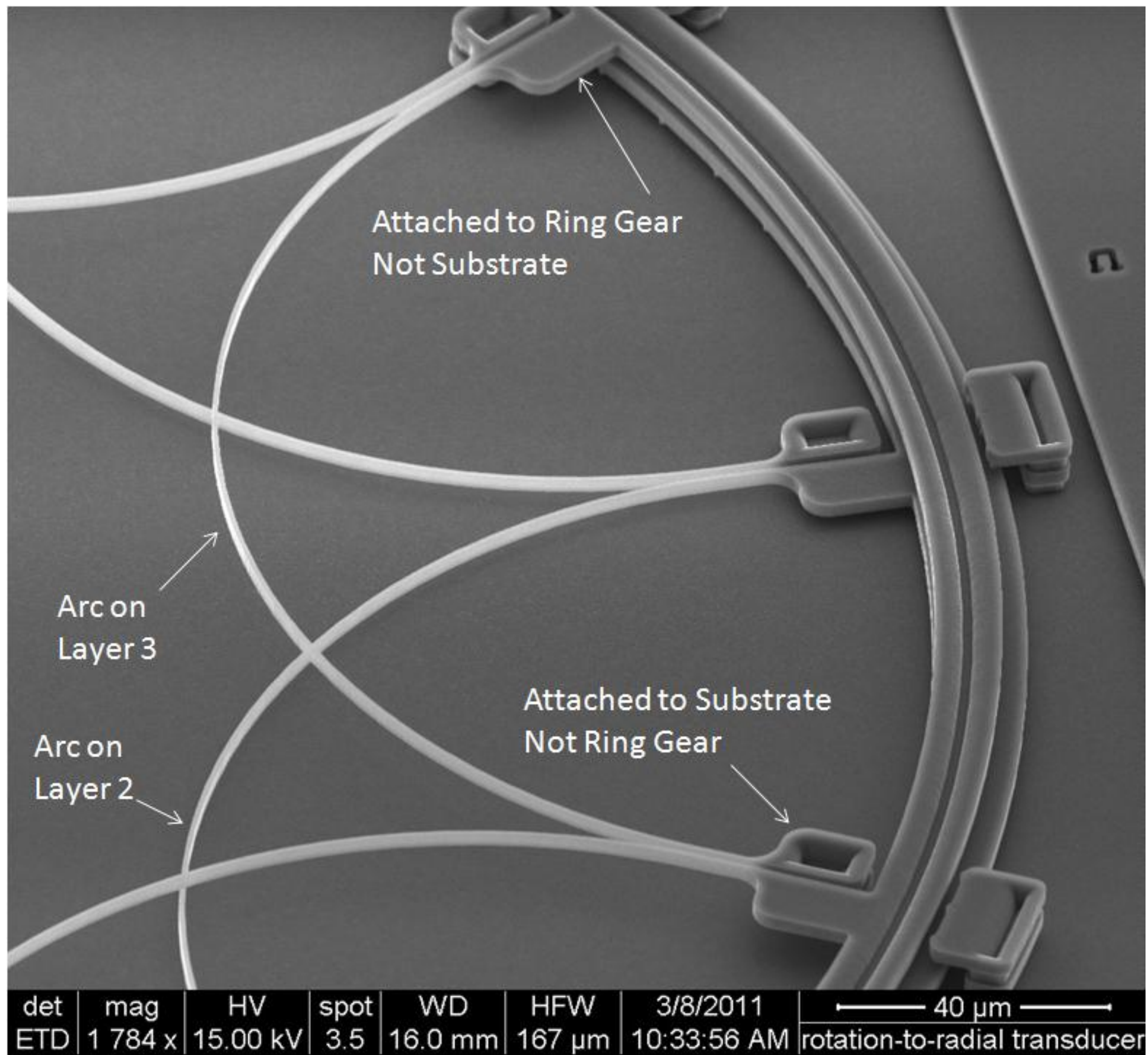

Figure 34. Electron micrograph of the as-built compliant arcs. The arcs on layer 3 cantilever 2.25 µm above the compliant arcs on layer 2.

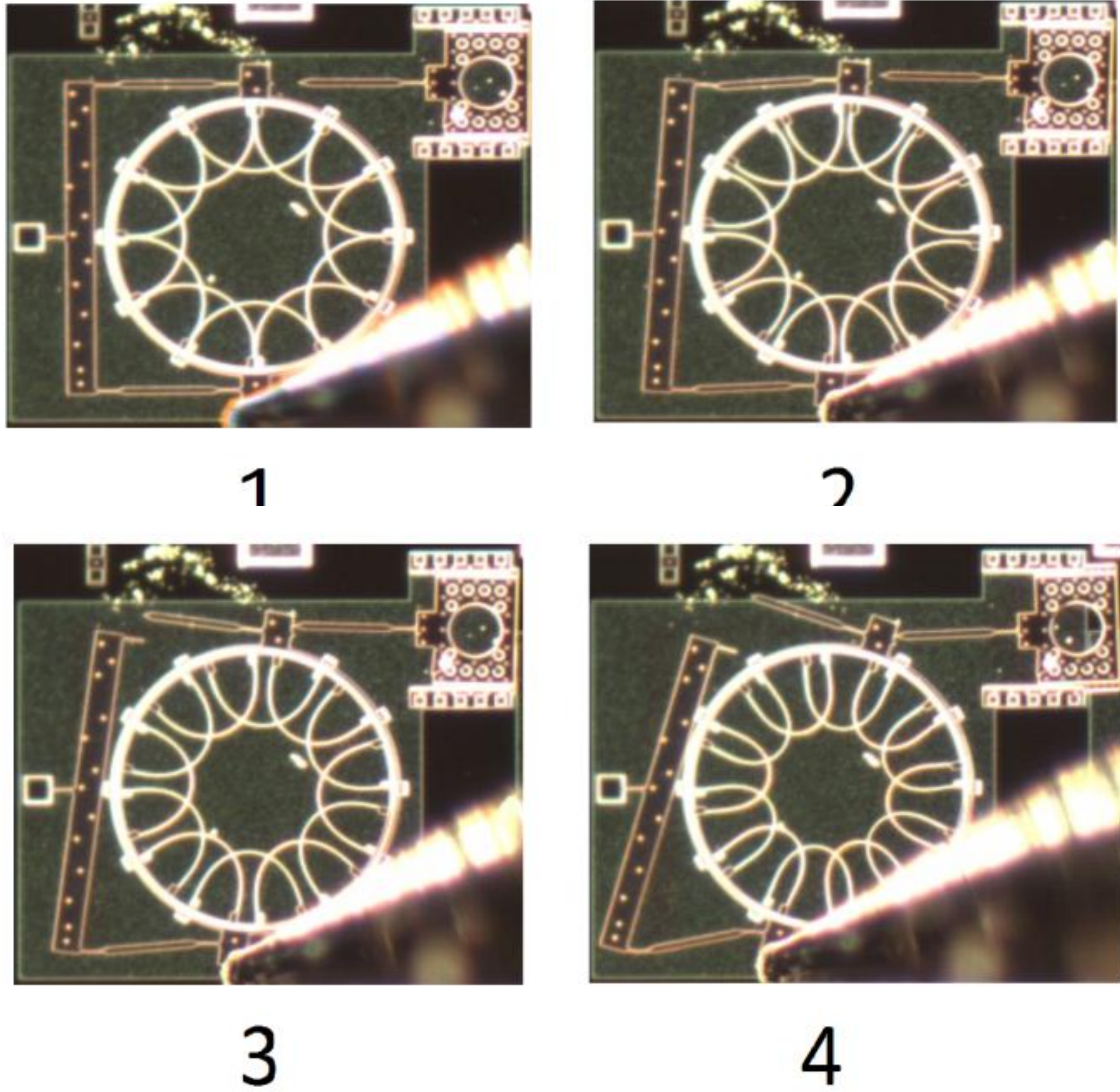

Figure 35. Sequential images of a radial motion transducer actuated with a probe tip [40].

The deflection ratios of each arc in the experiment agree with the finite element model and serve as validation. The data in Figure 36 lay within 5% of the numerical curve predicted by the finite element analysis. The experiment demonstrates that the compliant radial motion transducer is a viable mechanism and the assumed boundary conditions shown in Figure 30 accurately model the system when the input displacement is less than 16 µm.

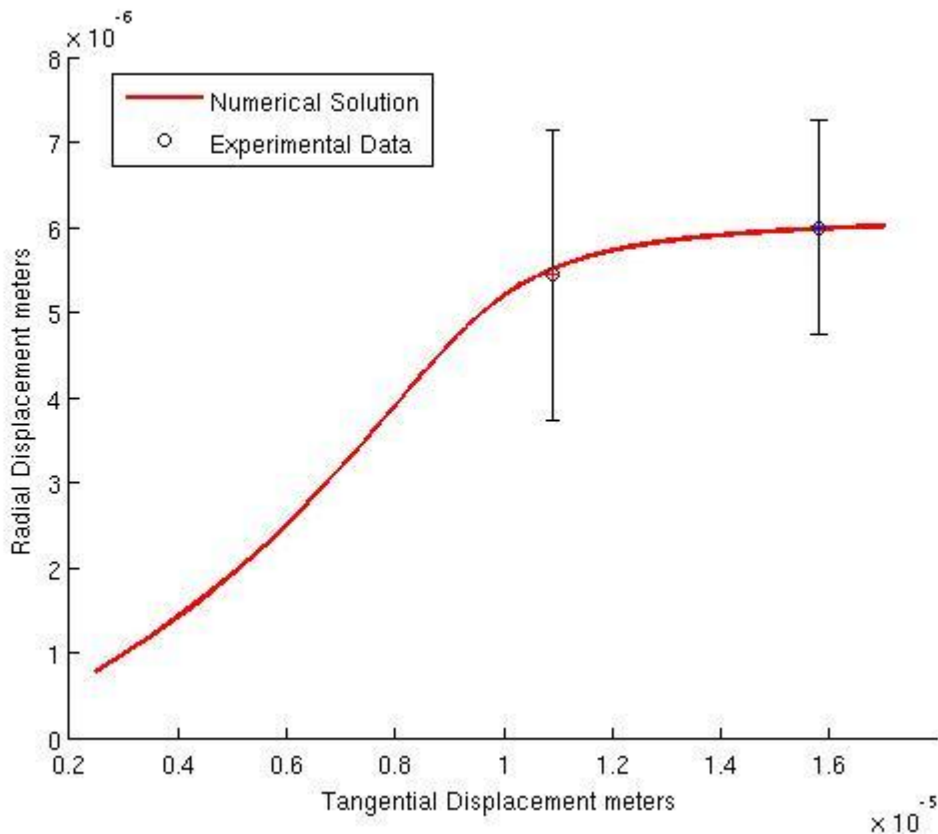

Figure 36. Experimental arc translation ratio compared to numerical results. Experimental data compared to the simulation of the input motion versus the output motion normal to the crest of the curve. Each data point corresponds to 24 redundant measurements (two for each arc in the ring gear) that are averaged. The standard deviation of each data set is represented by an error bar.

CHAPTER 5

CASE STUDY – PROBELESS SPIRAL SPRING ACTUATOR

Like in-plane linkages with pin joints, out-of-plane compliant mechanisms do not need to be constrained to systems with rigid components and flexible hinges. This case study presents a compliant actuator that achieves out-of-plane motion without a hinge or a rigid body apparatus. The actuator is a spiral spring with a constant pitch that starts from the outside diameter of a circle and moves to the center. The beams are 4 μm wide (virtually minimum dimensions for curved features in this architecture) and 2.25 μm thick. Figure 37 gives the dimensions of the spiral [41].

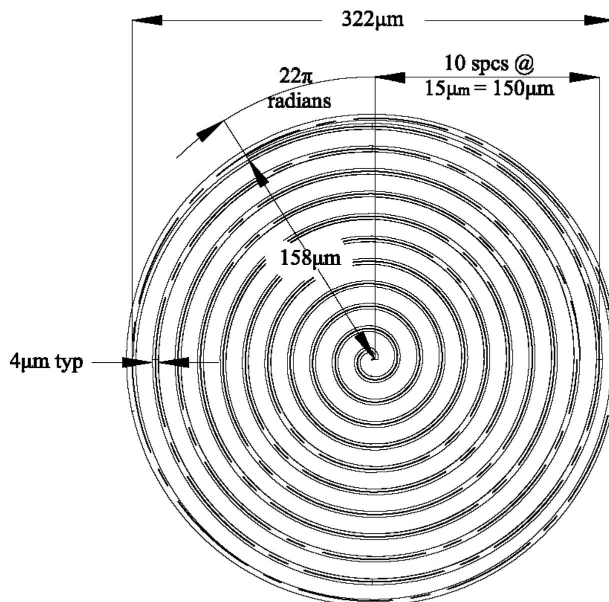

Figure 37. Center-line dimensions of spiral face and the beam width.

Other compliant out-of-plane actuators have been reported. In some cases, the stroke is limited to the distance between initial electrode spacing [43,44]. Electrostatic repulsive actuators have been reported that do not depend on initial electrode spacing [45-49]. These devices, however, utilize rigid electrodes connected to compliant hinges. The spiral actuator presented here achieves its motion through charge-pumped repulsion of a surface micromachined layer in a cantilever configuration. The stroke is not limited by initial electrode spacing and it uses no rigid members.

Sandia National Laboratories manufactured the actuator in the first three layers of the SUMMiT-V™ process [31,6]. The bottom layer, Layer-0 is a fixed 0.3 μm layer of polysilicon that lies on a dielectric foundation. Layer-1 is a 1 μm thick conductive polysilicon layer built up on a 2 μm layer of sacrificial silicon oxide to create a separating gap between the bottom plane and the actuator. The outer ring of the spiral is affixed to the substrate. Layer-2 is laminated with layer-1 in the center of the spiral (Figure 38) [5,6].

The laminate layers in the spiral arms are separated by a 0.3 μm gap left by uncut silicon oxide. Connection points between the two layers constrain the two layers and they share deflection as two spring in parallel. In Appendix B, conservation of energy and a parallel spring assumption are applied to show that the spring constant of the system is at least 9 mN/m. Figure 39 is a cross-section of the spring actuator that shows the top and bottom layers connected.

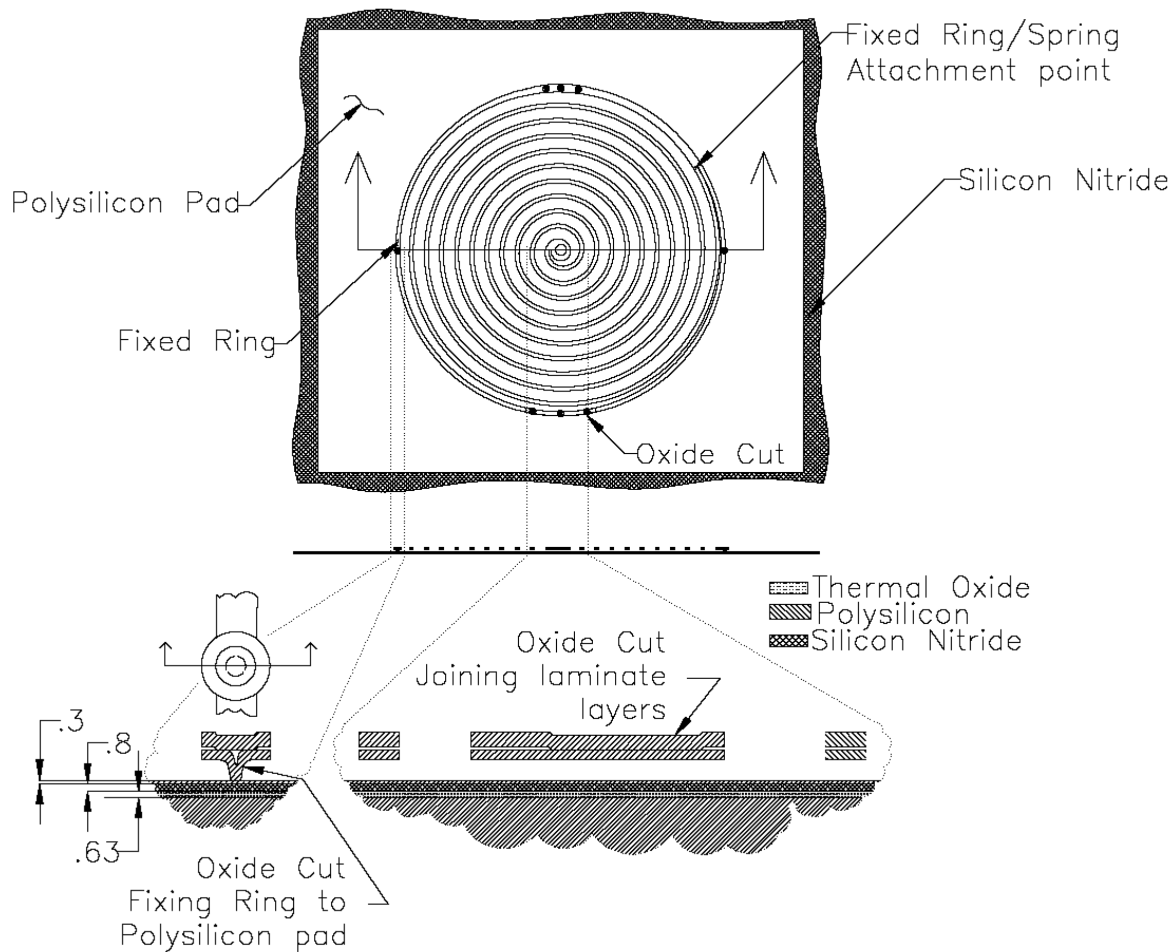

Figure 38. Architecture of the spiral spring actuator. Cross-section cut shows the laminated layers, 1 and 2. It also shows the oxide cut which fixes the outside ring to the substrate.

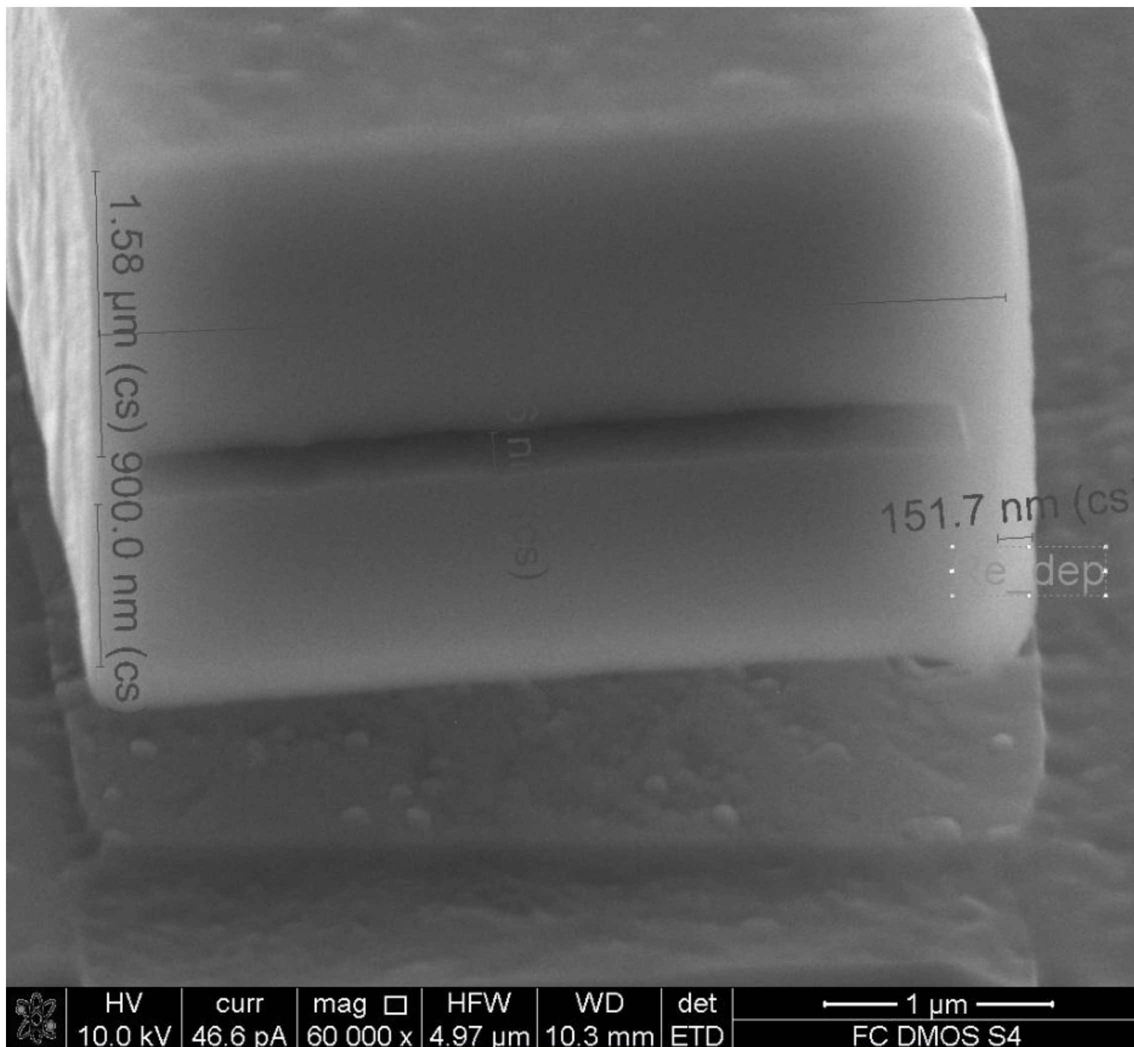

Figure 39. Cross-section of the spiral actuator. The cross-section was taken at the outside ring attachment to the substrate. The gap in the center is a result of silicon oxide taken out of the process before release. This cross-section is cut by focusing ions in a focused ion beam (FIB) microscope. The cross-section shows the top and bottom layers connected.

The center of the ungrounded actuator deflects out-of-plane when subjected to dynamic charge injection by the scanning electron microscope. Like the plate and slider-rail actuators (described in Chapter 2) the actuation force that acts on this device depends on imaging conditions (magnification, beam current, scan rate, and accelerating voltage).

The spiral consistently deflects as though it is acted upon by a nearly uniform distributed load.

Figure 40 and Figure 41 show two experimental data sets compared to a finite element simulation that assumes a uniform pressure normal to the bottom of the spiral. The model uses 28k geometrically nonlinear solid elements in COMSOL[6] [42]. The finite element model predicts a deflection that is within 5% of the deflection observed in the experiments.

Figure 42 compares the deflections predicted by the nonlinear COMSOL simulation to the linear spring constant from Appendix A and verifies the finite element analysis.

---

[6] We chose COMSOL solid elements to solve this problem rather than beam element because the mechanics simulation is part of a more comprehensive multiphysics simulation of dynamic charge actuation. The nonlinear simulation uses the Green-Lagrange strain and the second Piola Kirchoff stress to calculate large deflection [42].

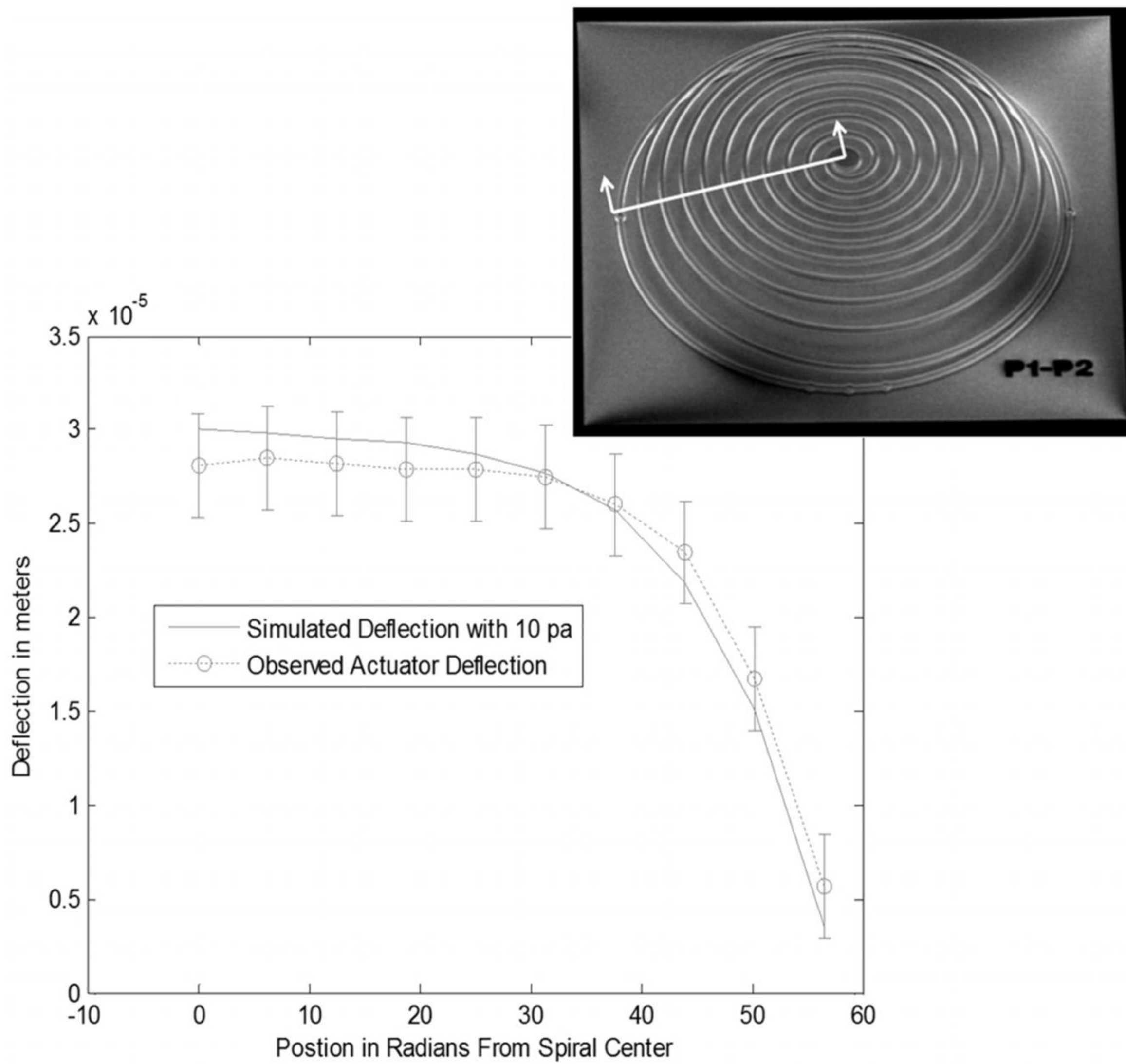

Figure 40. Deflection measurements taken from a cross-section of the spiral stretched 30 μm out-of-plane. The deflection corresponds to an equivalent 267 nN point load (pressure multiplied by spiral surface area).

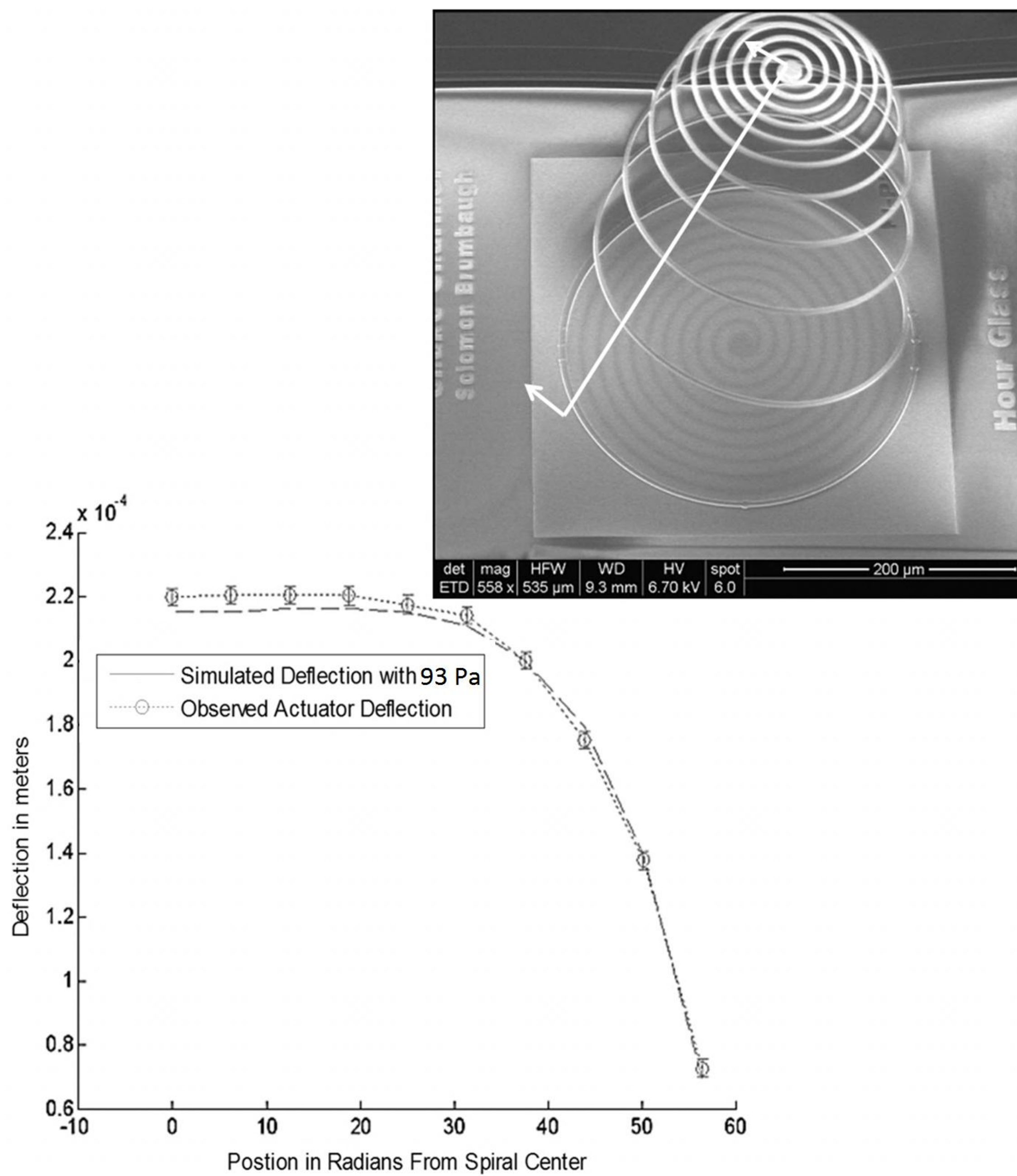

Figure 41. Largest deflection of the spiral. The spiral raises out-of-plane to produce a 220 µm stroke that corresponds to an equivalent 2 µN point load (pressure multiplied by spiral surface area).

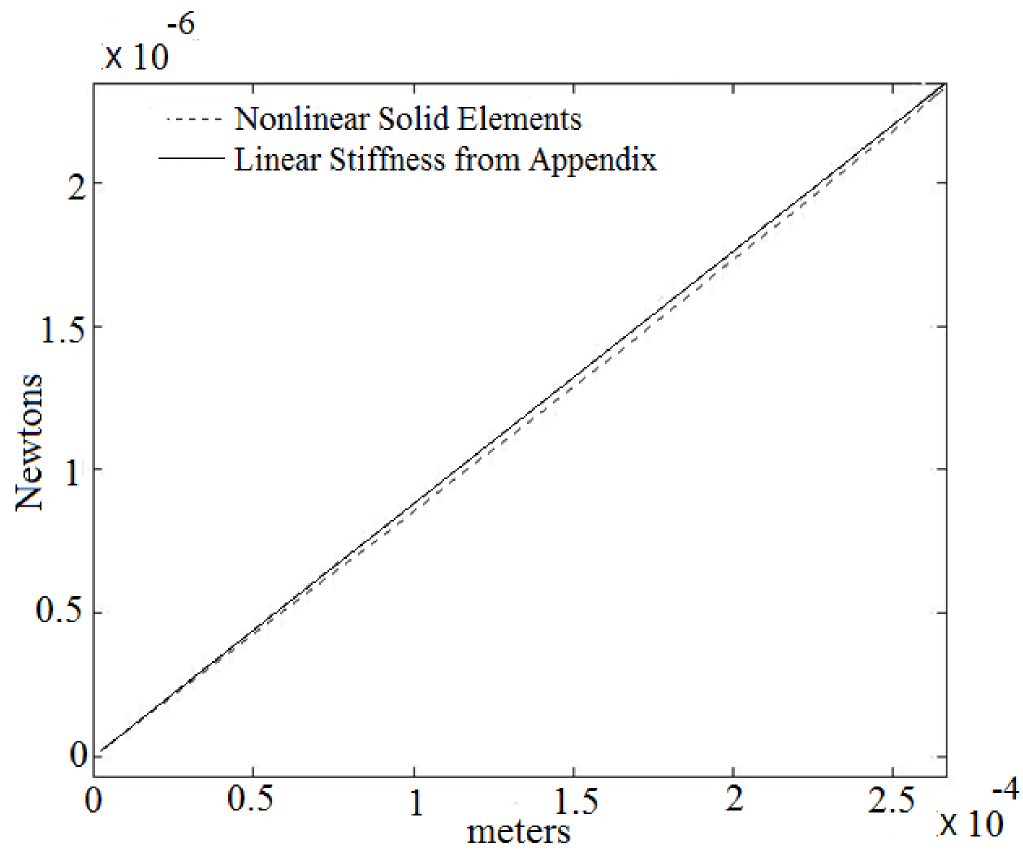

Figure 42. Nonlinear finite element solution compared to linear stiffness. The agreement between the analytical linear stiffness and nonlinear COMSOL code verifies that COMSOL solves the governing equations correctly.

CHAPTER 6

CONCLUSIONS

6.1 Observations and Conclusions

This thesis demonstrates that frictional contact in micropin joints and hinges is an encumbrance in microsystems that can be eliminated by use of compliant mechanisms. After comparing compliant torsion springs to the substrate hinge, assessing the practicality of an out-of-plane microcompliant bistable mechanism, investigating the compliance limit for out-of-plane compliant actuators, and developing a compliant alternative to a rigid body linkage in a ring gear, this research concludes that:

- Compliant hinges will repeatedly twist 90° out-of-plane. Parallel and series beams in torsion enable out-of-plane motion at least as large as is possible through use of classical MEMS substrate or scissor hinge designs.
- A bistable-compliant elastic hoop is a compliant threshold hinge that acts out-of-plane under a manual torsion load. The torsion load flips the elastic ring inside-out and proves that it has a second stable state.
- A compliant linkage translates rotational-to-radial motion similar to its rigid-body counterpart without the use of pin joints and sliders. A total Lagrangian finite element analysis validated by experimentation shows that a micro-compliant arc with a 100 µm radius of curvature can convert a 16 µm horizontal

- displacement into a 6 μm deflection at the crest of the arc. In a ring gear, this compliant arc can be used to translate a 10° twist to a 6 μm radial displacement (16% of the initial ring gear radius), which corresponds to 7 mN tangential force per arc on the ring gear. The compliant arc translates motion with a 0.64 μm/μm ratio until 11 μm, whereupon the translation ratio reduces to 0.023 μm/μm.
- A spiral spring actuator deflects 70% of its largest lateral dimension (220 μm).

6.2 Contributions

The material in this thesis has generally contributed to the scientific community by presenting new micromechanical designs that include:

- A microcompliant rotational-to-radial motion transducer.
- A microcompliant bistable mechanism that acts out-of-plane.
- Characterization of an out-of-plane spiral spring actuator.
- Out-of-plane rigid plate and beam actuators (compliant torsion hinges).

Furthermore, models were presented that describe the behavior of the microcompliant mechanisms. The models include:

- A total Lagrangian curved beam finite element MATLAB code for a fixed/guided, curved cantilever beam.
- An ANSYS script of a torsional bistable mechanism with artificial damping to approximate snap through. The artificial damping under-predicts torsion. It must therefore be crosschecked with a model that does not use artificial damping.
- An efficient closed form linear model of the spiral spring actuator is presented with a MATLAB script to calculate stiffness.

- Finally, a MATLAB script to run a nonlinear finite element model of the spiral spring actuator in COMOSL has been developed. The mechanics model can be coupled with Maxwell's equations using an ALE mesh and the multiphysics capabilities in COMSOL to study charging effects.

7 CHAPTER

FUTURE WORK

7.1 Future Development of Compliant Rotation-to-Radial Motion Transducer

The compliant motion transducer requires an unachievable actuation force given current MEMS actuation techniques, and its radial motion is limited by stress stiffening that decreases the motion translation ratio to 0.023 μm/μm (see Figure 31). This raises the question: How can the actuation force be reduced and the translation ratio increased?

The stress stiffening could be reduced and the radial motion magnified if the tangential force corresponded to the crest deformation. Ideally, a configuration could be created that would generate an exact inverse to the current translation ratios. A future design might use compliant arcs that are oriented perpendicular to the current orientation. Fastened in parallel, the compliant arcs would amplify tangential motion in the radial direction (Figure 43).

In addition to low translation ratios, the rotation of the ring gear in the motion transducer (Figure 28) necessitates a component of motion perpendicular to the radial direction (Figure 44). In a practical application, such as a biomimetic accommodating focus mechanism in a camera, the perpendicular component of motion would produce a torque that might introduce optical aberrations in the lens. A symmetric load on both ends

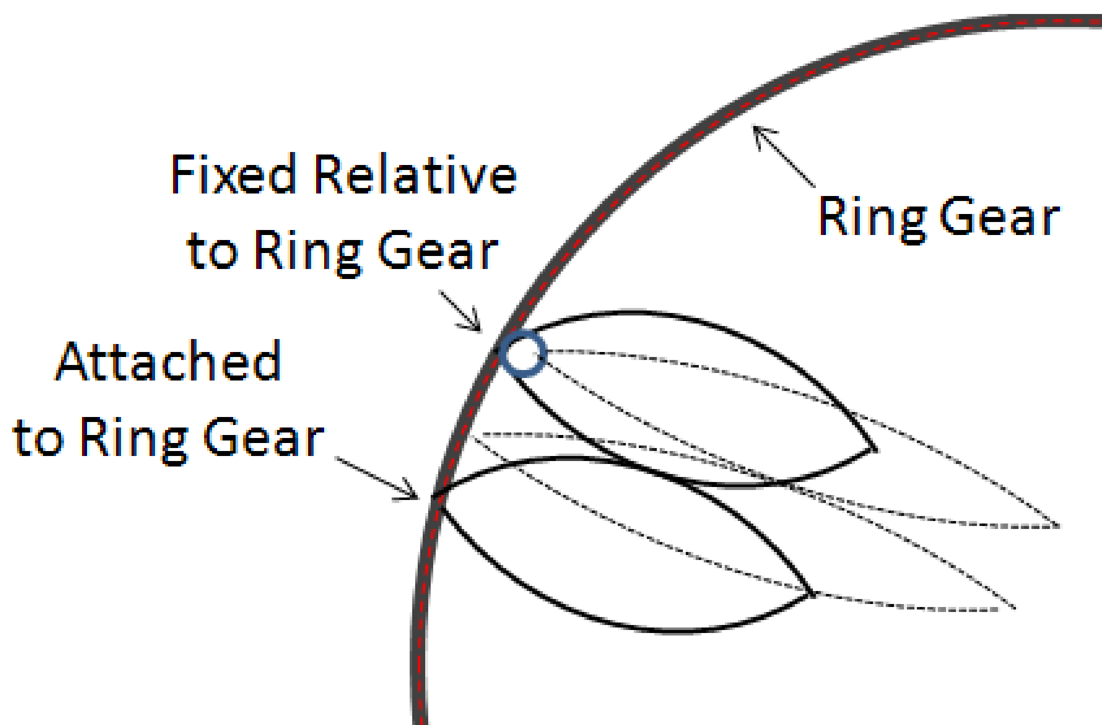

Figure 43. Compliant arcs loaded at the crest by a ring gear. Shallow arcs arranged in an oval shape do not eliminate stress stiffening; however, the ovals amplify radial motion so that a smaller twist translates to larger radial motion. New or existing MEMS actuators can be used to actuate the ring.

of the compliant arc would eliminate this problem. If the ends of the compliant arc were fixed to two concentric ring gears that rotate opposite of each other, the crest of the microcompliant arc would only move in the radial direction.

Hence the question is raised, how can superimposed ring gears be used to impart a symmetric load on compliant arcs in a surface machine process without re-introducing the very problems of contact we are attempting to avoid?

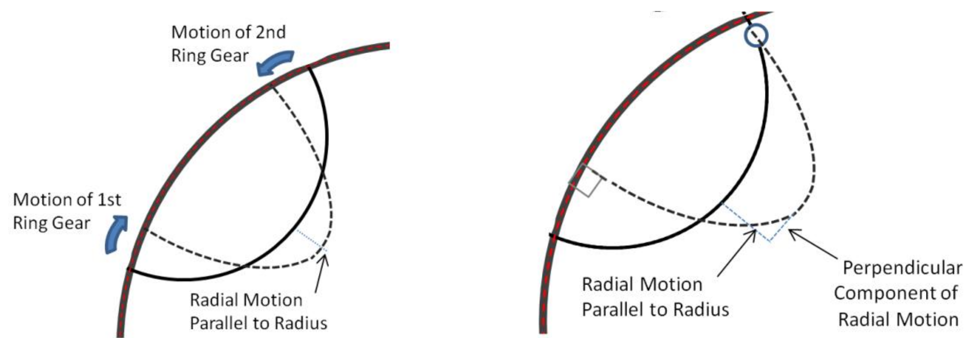

Figure 44. Radial motion of the compliant arc has a perpendicular component. The perpendicular component of motion may presents aberration problems to variable optic applications for such a mechanism. Superimposed ring gears moving opposite of each other would squeeze the arc symmetrically, eliminating the perpendicular component of radial motion.

7.2 Future Development of Bistable Compliant Hoop

In addition to in-plane mechanisms, out-of-plane mechanisms are also analyzed. Numerical simulations have shown that not all micro-elastic compliant hoops are bistable. Is there a general relationship that exists between the radius of curvature, cross-section dimensions, and material properties that could provide insight into the stability of an elastic hoop?

As mentioned in Chapter 4, flattening the curvature of the elastic hoop shifts the snap through point. Numerical simulations have shown that changing the modulus of elasticity or the moment of inertia does likewise. Observations of an elastic ring have shown that the bending component of the deformation is the last part to snap inward. How does bending stiffness affect the stability of an elastic ring? Does the change in the stability point represent the introduction of tensile stress 90° from the concentrated torsion or is it the reduction in bending moment caused by less curvature?

Furthermore, the microcompliant bistable elastic hoop uses a constraint strap to concentrate the imparted moment about the centroid of the cross-section. The constraint strap introduces contact between the elastic hoop and the strap. Further investigation might answer the following questions: How can a concentrated torsion be applied about the cross-section of an elastic hoop without the use of a constraint strap? Without the constraint straps, how can the elastic hoop be preserved during fabrication?

The plate and beam actuators used to test the compliant hinges in Figure 13 and Figure 19 could be applied to an actuator that would stand an elastic hoop out-of-plane and turn it inside-out without a constraint strap. Actuators like this have not been shown to move through such complex trajectories. However, there is nothing to indicate that they could not do it. The governing principles of these actuators are not known. What are the limits of dynamic charge injection?

7.3 Overview of Dynamic Charge Injection

While it is beyond the scope of this thesis to characterize the attributes and relative usefulness of dynamic charge injection, many of the components presented here make use of it. Critical analysis of these experiments has lead to perplexing observations and unresolved questions.

Experiments on the spiral spring actuator have shown that dynamic charge injection consistently deflects the spring 30 μm, implying that the technique generates 52 N/μm (13 Pa) on beams 4 μm wide and 15 μm apart. In the same experiment, the working distances were varied between 68 mm, 50 mm, and 10.4 mm to see that working distance does not affect actuation. Furthermore, varying the voltage bias on the secondary electron

detector from -239 V to 260 V showed that actuation does not depend on voltage bias of the secondary electron detector. If the electron beam stops scanning or is turned off, the spiral spring lays down.

Accelerating voltage also affects the actuator and must be set between 5kev and 9kev to produce a deflection. Increasing magnification increases the stroke of this actuator. When magnification, accelerating voltage, and scan rate are adjusted in accordance with observed behavior, the spiral spring configuration deflects 220 μm. This implies that an equivalent uniform loads as high as 390 N/μm (97 Pa) can act on the spiral. Similarly, the plate actuator in Figure 13 consistently generates an equivalent 9 μm follower load (170 Pa).

Other experiments using variations of the spiral spring actuator reveal the truly dynamic nature of the charge injection technique. For instance, slight differences in architecture change the behavior of the spiral spring actuator and reveal stable vibration modes.

Figure 45 shows two spirals 2.25 μm thick connected at the rim, which are in turn connected to the center of a spiral identical to that of the case study. In steady-state, this actuator stretches into a spherical dome shape. The spherical shape is reminiscent of a repulsive system because objects dominated by uniform repulsion tend to stretch into spherical shapes (like a balloon filled with an ideal gas). The stretching in the dome-shaped spiral is not quasi-static: the repulsive pressure changes with time causing forced vibration. The wavy edges of the spring in

Figure 45 show a low vibration mode in the dome spirals, subject to scan speed.

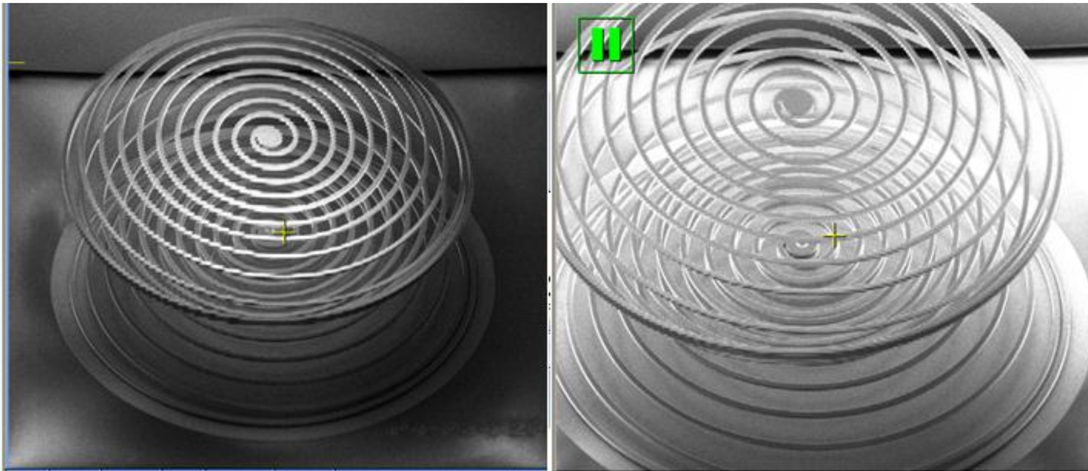

Figure 45. Dome shaped spirals actuated by charge injection. Three spiral spring actuators connected in the center and along the edges to see if they would make a dome shape upon actuation. The top two springs are 2.25µm thick made in layers 3 and 4 of SUMMiT-V™ [41].

Vibration modes in dynamic charge-pumped actuators depend on the imaging conditions and architecture. In Figure 46, a system of two spirals in an hour-glass shape vibrates violently. A decrease in the magnification, however, stops the vibration. The bottom left caption of Figure 46 shows the disparity between the vibrating mode and the quasi-static mode. A video of the transition between the vibration and quasi-static state can be seen at [50].

All of the actuators that use dynamic charge injection in repulsion mode are isolated conductors, with electrically interconnected components. For repulsive forces to exist on these electrical conductors, there must be a voltage gradient that either moves charge or effectively holds a stable net charge state. The source and magnitude of a voltage gradient has not been identified on these devices. The boundary conditions are not known and a model that associates the imaging parameters to actuation force is yet to be developed.

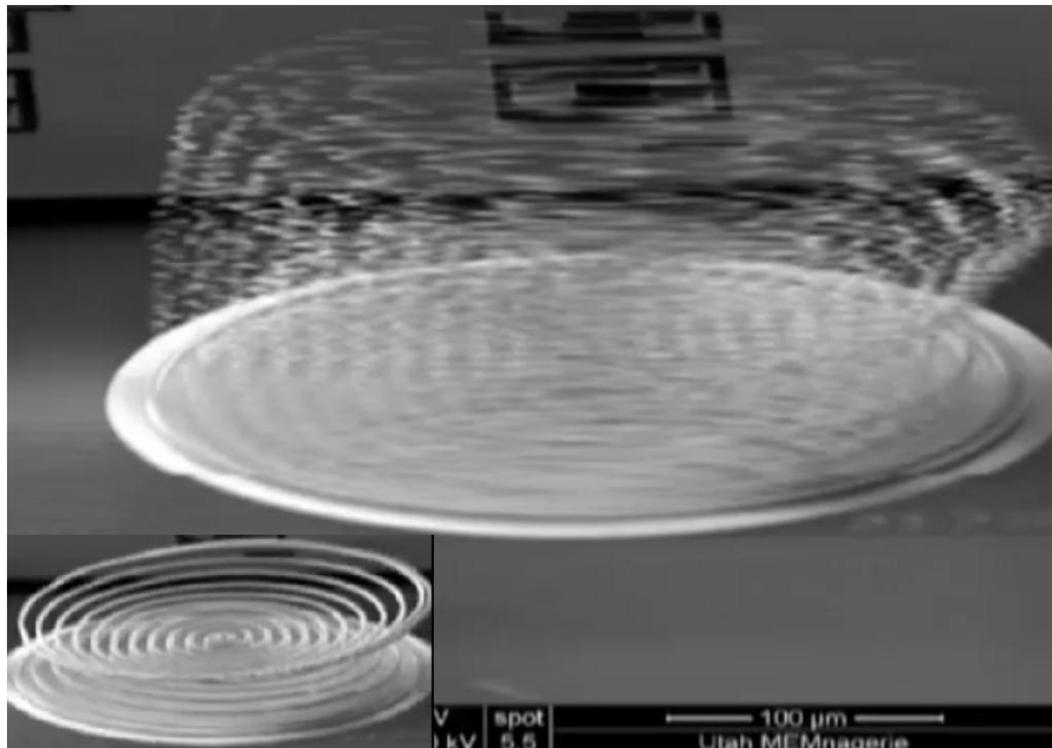

Figure 46. Two spirals connected in the center vibrating violently. The spiral vibrate violently before they reach steady state and maintain a constant deflection with the constant input electron flux. The bottom left shows the constant deflection achieved seconds after the vibration [41,50].

In conclusion, the experiments in this thesis have shown the following about dynamic charge injection:

- The actuation scheme does not depend on working distance, or bias voltage of the secondary electron detector.
- Actuation does depend on accelerating voltage, electron beam flux, and scan rate.
- Charge drains from the actuators, presumably into the vacuum and into the substrate.
- The actuation scheme produces equivalent uniform loads between 10 Pa and 170 Pa.

The above conclusions lead one to ask:

- Where does the charge drain to?
- What is the role of scan rate?
- What is the correlation between electron beam flux and scan rate?
- Why do certain actuators vibrate (what is the interaction between system compliance and dynamic charge/discharge state)?
- How does a grid of beams compare to a solid plate?
- Is there an optimum spacing between the arms of a spiral spring actuator that maximizes force and displacement?

Answers to these questions might establish a set of boundary conditions that could be used to numerically solve Maxwell's equations and better understand the dynamic charge injection technique and answer the question: How can the new charge-pumping actuation mechanism—which demonstrates promise for high force, large displacement—be

adapted for use in driving useful micromachines? For example could the actuation technique be refined to actuate the complaint rotation-to-radial motion transducer or other high force devices?

APPENDIX A

ANSYS CODE TO SIMULATE A BISTABLE ELASTIC HOOP

```
FINISH
/CLEAR,start
/TITLE,Bistable Ring
/FILNAME,zzz_bistable,ON
/UIS,MSGPOP,3
/UIS,abort,off
!****************************************
! Inputs for geometry and loads
!****************************************
! Units are microns, milligrams, milliseconds
! Force in microNewtons  Stress/Modulus in MPa
circRad=350     ! Radius of Elastic Hoop
thickness=2.25  ! out-of-plane thickness
width=1         ! in-plane width of arc
yMod=160000   ! Young's Modulus
pRat=0.25         ! Poisson's Ratio
numElem=100   ! Number of elements
numCrossElem=20! cross section stiffness
numLoadSteps=20 ! Number of loads steps
stabDamp=0.0005  ! Artificial Damping Const

/prep7
EMUNIT,EPZRO,8.85399999845E-06
PI=3.14159265359
*afun,deg

! Create Geometry
k,1,0,0,0
k,2,circRad/10,0,0
circle,1,circRad,,2,90

! Set up elements
ET,1,BEAM188
keyopt,1,3,2 ! use quad shape function
SECTYPE,1,BEAM,RECT,beamRect,0
SECOFFSET,CENT
SECDATA,width,thickness,numCrossElem,numCrossElem,0
,0,0,0,0,0

! Set up material properties
MP,EX,1,yMod
MP,PRXY,pRat

! Mesh beam
esize,,numElem
mat,1
secnum,1
type,1
lmesh,all

! Apply boundary Conditions
ksel,s,loc,x,0
ksel,r,loc,y,circRad
*get,kpSym,kp,0,num,max
nslk,s
*get,nSym,node,0,num,max
ksel,s,loc,x,circRad
ksel,r,loc,y,0
*get,kpLoad,kp,0,num,max
nslk,s
*get,nLoad,node,0,num,max
allsel,all
dk,kpSym,ux,0
dk,kpSym,roty,0
dk,kpSym,rotz,0
dk,kpLoad,ux,0
dk,kpLoad,uy,0
dk,kpLoad,uz,0
dk,kpLoad,rotx,0
dk,kpLoad,rotz,0
dk,kpLoad,roty,-PI !! Apply 180 degree rotation

! execute solution
finish
/solu
antype,static
nlgeom,on
outres,all,all
nsubst,numLoadSteps,numLoadSteps*1000,numLoadSteps
*if,stabDamp,ne,0,then
  stabilize,constant,damping,0.0005,no
*endif
neqit,200
keyw,pr_sgui,1 !suppress solution is done note
allsel,all
solve
keyw,pr_sgui,0 !reset command after solve

! Post process results
finish
/post1
!/ESHAPE,1.0 ! uncomment to see beam as 3D solid

! Post process using time history
FINISH
/POST26
RFORCE,2,nLoad,M,Y, MY_2
STORE,MERGE
XVAR,1
PLVAR,2,
```

Main file to simulate a Compliant Arc in GESA (MATLAB)

```
%------------------------------ Executes GESA DO NOT CHANGE---------------------------
format short, clear all,  close all
global E A MGTYPE XYZ CONNEC TR0 CTOL TR GAUSSP GAUSSW GAUSSX3 GAUSSN3 GAUSSW3 NE NN NDF global
NTT BCDOF NBC DOF NEQ NLAYER PHIS PHIMS ELE_TYPE  NUMBERN  LUMPM  LUMPK LOAD0 LOAD global
LOADD LOADP lda CONTROL0 CONTROL1 OUT DISPANG  DISPDIM
BC=[]; BCC=[];  LOAD0=[]; LOAD=[]; LOADP=[]; LOADD=[]; LOADF=[];LUMPM=[]; LUMPK=[]; PHIS=[]; PHIMS=[];
DISPANG=[20 40];[GAUSSP,GAUSSW,GAUSSX3,GAUSSN3,GAUSSW3]=gauss; CTOL=1.0e-10;
ELE_TYPE={'eTruss23','eBeam26','eBeam28','eMembrn43','eMembrn43q'
'ePlate45','ePlate46','ePlate47','ePlate36','eSolid83','eTruss23n','eCable23n','eBeam29n''eBeam26v','ePlate412n','ePlate46v','eShell414n
','eMembrn43n','eMembrn33n','eMembrn83n'};   NUMBERN=[2 2 2 4 4, 4 4 4 3 8, 2 2 2 2 4, 4 4 4 3 8]; DISPANG=[0,0];
%--------------------------------Compliant Arc Parameters-------------------------------
angle = 126;  % Angle of arc in DEGREES
   R = 100e-6 % Radius of curvature in meters
  NE = 16;   % Number of elements should always be an even number
  NN = ne+1;  % Number of nodes
%------------------------------------- Generate Mesh ------------------------------------
%          use eBeam29n elements (nonlinear beam elements)
curve2(1,1,13,[R 0 0],[0 0 0],[R 0 R],angle,NE);
%          curve2 always generates the mesh such that the cross section of the
%          first node is parallel to the global x axis accordingly
 [XYZ,TR] = arc_rotator(XYZ,TR);  % This function reorients the mesh so that node 1 and
                     % and node NN both align with the global x axis.
                               % function[XYZ_rotated, TR_rotated] = arc_rotator(XYZ,TR);
                               %   [NN,trash] = size(XYZ);  theta = atan(XYZ(NN,3)/XYZ(NN,1));
                               %   T = [ cos(theta)  0  sin(theta)
                               %          0    1      0
                               %       -sin(theta) 0   cos(theta) ];
                               %   for i = 1:NN, XYZ_rotated(i,:) = (T*(  XYZ(i,:)'))';end
                               %   for i = 3:3:3*NN
                               %                dummy_row = ((i-3)+1):(3+(i-3))
                               %               TRo(1:3,1:3) = TR(dummy_row,1:3)  ;
                               %                TRo_rotated = T*TRo;%*(T')   ;
                               %      TR_rotated(dummy_row,1:3) = TRo_rotated(1:3,1:3)  ;
                               %   end
                               % end
%-------------------------- Material and geometry properties-----------------------------
%                 Generates [D] Matrix from appendix A
NMAT=1; E=zeros(NMAT,10); %total number of materials, material property matrix
e=160e9; nu=0.25; rho=0.2507; E(1,[1 4 10])=[e, nu, rho]; %Young modulus, Poisson
NGEO=1; A=zeros(NGEO,2); %total number of element geometries, geometry property matrix
b=1e-6; h=2.25e-6; area=b*h; I22=b*h^3/12; I33=b^3*h/12;
nn=[1:2:200]; xx8=tanh(nn*(pi*b/h/2))./(nn.^5); I11=b*h^3/3*(1-192*h/b/pi^5*sum(xx8));
c1=0.83333; c2=c1; c3=0; c4=I11/(I22+I33); %correction factors for warping
k1=0; k2=1/R; k3=0; %initial curvatures
A=[area,  c1,c2,c3,c4,k1,k2,k3,1,0, -b/2, -h/2,b/2, h/2, 1];
%---------------------------------- Boundary Conditions----------------------------------
NDF = 9        ; % max. number of DOFs per node of all elements used in the FE model
BCC = zeros(NN,NDF); % for indicating each DOF's status: 0=free, 1=fixed
%    Fixed Guided at Node 1        End Node Fixed        % Reduce to 2d Problem
    BCC(1,[2,3,4,6])=1;          BCC(NN,[1:9])=1;      % BCC(:,[2 4 6 8 9])=1;
LOAD(1,:)=[1,1,15e-4];             % Apply Point load in global x direction
OUT=[((NN/2)+.5),3;((NN/2)+.5) 1;1,1];  % output [node number, nodal DOF; ...]
%------------------------------------- Solver Controls ---------------------------------
   lda = 0  ;      ldamin = .015;       ldamax = 36  ;     Dlda = .02   ;
 Dldamax = .2 ;       Dqmax = 1.0 ;            qmin = -200;    qmax = 160e-6;
 lsmax = 600;      itrmax = 30  ;            nr = 5  ;     tol = 1.0e-4;
CONTROLO = [lda,ldamin,ldamax,Dlda,Dldamax,Dqmax,qmin,qmax,lsmax,itrmax,nr,tol,0];,
    NTT=NN*NDF; q=zeros(NTT,1);        % initial displacement
% ------------------------------- Start Solver-----------------------------------------
  NonlinearStatic1
```

APPENDIX B

LINEAR SPRING CONSTANT OF THE SPIRAL SPRING ACTUATOR

The linear spring constant in the spiral is found by calculating the total elastic energy that an arbitrary, uniform load imparts on the spiral. The spiral shape is approximated by 53 quarter-arc segments with constant curvature. The constant curvature of each arc is calculated by taking the average curvature of the spiral in 90° increments. Each arc is assumed fixed at one end and free on the other. The arcs are loaded by a uniform load per length *w,* a bending moment *Mo*, torsion *To,* and point load *P,* as shown in Figure 47. Boundaries, *Mo, To,* and *P* on each arc are found by integrating the loads on preceding arc elements. The concentrated end loads *Mo, To,* and *P* are assumed zero on the first arc element.

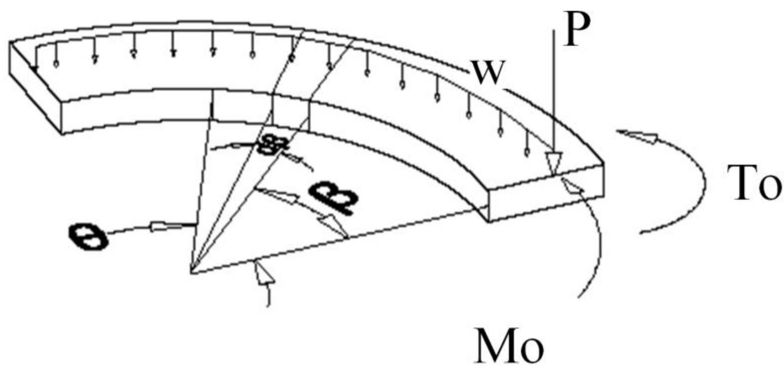

Figure 47. Assumed loading on an arc element in the spiral.

The total strain energy in the spiral can be expressed in terms of the angle θ and an index variable i that represents each arc element [20]. Equation (8) assumes that all of the strain energy is due to bending and torsion.

$$\sum_{i=1}^{n} \Pi_i = \int_{\theta_{initial}}^{\theta_{end}} \left(\frac{{M_{Total_i}}^2}{2EI} + \frac{{T_{Total_i}}^2}{GJ}\right) R_i d\theta \tag{8}$$

Since each arc is a quarter circle, the boundary conditions $\theta_{initial}$ and θ_{end} of the integral in equation (8) increases in $\frac{\pi}{2}$ increments. The angles are expressed in terms of the index variable *i* in equations (9) and (10).

$$\theta_{initial} = \frac{\pi}{2}(i-1) \tag{9}$$

$$\theta_{end} = i\frac{\pi}{2} \tag{10}$$

On each arc element, loads *P*, *w, Mo,* and *To* exert moment and torsion on a differential element dθ that varies with θ. To account for the torsion and moment of the distributive load *w*, we define a pseudo angle β between 0 and θ in Figure 48.

The differential element *dβ* has an arc length of *Rdβ* that exerts a force *wRdβ* . The distance between *θ* and *dβ* has perpendicular components *R(θ-β)* and *R(1-cos(θ-β)*). Force *wRdβ* acts parallel to the distance *R(1-cos(θ-β)*) and perpendicular to *R(sin(θ-β))*[20].

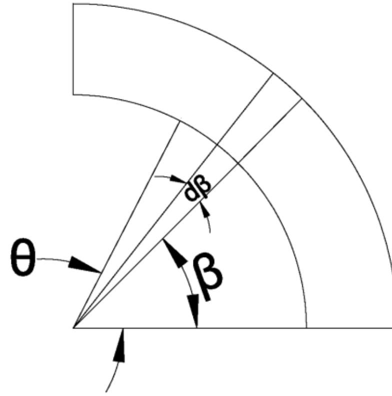

Figure 48. Top view of quarter arc segment shows the relationship between β and θ.

Therefore, the torsion component dT_q and bending component dM_q can be expressed as

$$dT_q = wR^2(1 - \cos(\theta - \beta))\mathrm{d}\beta \tag{11}$$

$$dM_q = w\, sin(\theta - \beta)\, d\beta. \tag{12}$$

Integrating equations (11) and (12) from 0 to θ yields a total torsion equation in terms of θ (equation (13) and (14)).

$$T_q = \int_0^{\theta} wR^2(1 - \cos(\theta - \beta))\mathrm{d}\beta \;\; = -wR^2(\sin(\theta) - \theta) \tag{13}$$

$$M_q = \int_0^{\theta} wR^2 \sin(\theta - \beta)\, d\beta \quad = -wR^2(\cos(\theta) - 1)\,. \tag{14}$$

The point load P exerts a moment on the differential element $d\theta$. At $d\theta$, load P is a perpendicular distance $R(1 - cos(\theta))$ and a parallel distance $PRsin(\theta)$ away. Consequently, the moment and torsion due to P is as follows:

$$M_p \;=\; PR(1 - cos(\theta)) \tag{15}$$

$$T_p \;=\; PRsin(\theta)\;. \tag{16}$$

The concentrated moment *Mo* and concentrated torsion *To* acting on the arc can be expressed in terms of θ by dividing each into perpendicular components along the arc. Hence, a moment *M* and torsion *T* at any point along the arc is given by equations (17) and (18) .

$$M \;=\; ToRsin(\theta) \;+\; MoR(1 - cos(\theta)) \tag{17}$$

$$T \;=\; MoRsin(\theta) \;+\; ToR(1 - cos(\theta))\;. \tag{18}$$

The total moment on a curved element is the sum of Equations (12),(14),(15), and (17) in equation (19).

$$M_{total} = ToRsin(\theta) + \ MoR\big(1 - cos(\theta)\big) - wR^2(\cos(\theta) - 1) + PR(1 - cos(\theta))$$

(19)

$$= R(Tosin(\theta) + \ Mo\big(1 - cos(\theta)\big) - wR(\cos(\theta) - 1) + P(1 - cos(\theta))$$

Likewise, total torsion in a curved element is the sum of equations (11), (13), (16) and (18) as is done in equation (20).

$$T_{total} = -wR^2(\sin(\theta) - \ \theta) + MoRsin(\theta) + \ ToR\big(1 - cos(\theta)\big) + PR(sin(\theta))$$

(20)

$$= R(Mosin(\theta) - wR(\sin(\theta) - \ \theta) + \ To\big(1 - cos(\theta)\big) + PR(sin(\theta))$$

The total moment M_{Total} and the total torsion T_{Total} depend on the loads of the proceeding arc. The torsion *To* moment *Mo* and point load *P* change with each element or index variable *i* along the spiral. P_i is found using sum of the forces in equation (21).

$$P_i = P_{i-1} + wR_{i-1}\frac{\pi}{2} \qquad (21)$$

Mo_i is the integral of the moment equation for all proceeding arc segments and To_i is the integral of the proceeding torque equation. Equations (22) and (23) show the integrals with their respective index variables.

$$Mo_i = Mo_{i-1} + \cdots$$

$$\int_{\frac{\pi}{2}(i-2)}^{\frac{\pi}{2}(i-1)} To_{i-1}R_{i-1}sin(\theta) + Mo_{i-1}R_{i-1}\big(1 - cos(\theta)\big) - wR_{i-1}{}^2(\cos(\theta) - 1) \tag{22}$$

$$+ P_{i-1}R_{i-1}(1 - cos(\theta))\ d\theta$$

$$To_i = To_{i-1} + \ \ldots$$

$$\int_{\frac{\pi}{2}(i-2)}^{\frac{\pi}{2}(i-1)} Mo_{i-1}R_{i-1}sin(\theta) + To_{i-1}R_{i-1}\big(1 - cos(\theta)\big) - wR_{i-1}{}^2(\sin(\theta) - \theta) \tag{23}$$

$$+ P_{i-1}R_{i-1}(sin(\theta))d\theta$$

The integrals in equations (22), (23), and (8) are evaluated numerically. The total strain energy Π_{Total} is a function of *w* and arc length *s*. The product of *w* and *s* make a cumulative point load that acts at some point on the spiral. A linear relationship between the cumulative point load and maximum deflection exist and is given by equation (24)

$$\frac{K\delta^2}{2} = \frac{F\delta}{2} = \frac{ws\delta}{2} = \Pi_{Total}(w,s) \tag{24}$$

The linear spring constant K that corresponds to the equivalent point load F, is found by solving equation (24). The resulting spring constant is provided in terms of geometric and material properties in equation (25)

$$K = \frac{2.99(10^{15})s^2 EIGJ}{969EI + 1465GJ} \tag{25}$$

The spiral spring actuator in Chapter 6 consists of 2 springs in parallel (layer 1, and layer 2). The spring constant of the lμm thick layer is .00209N/m and the spring constant of the 1.5μm thick layer is .00682N/m. The total spring constant of both layers together is .00891 N/m.

$$K_{eq} = .00682\frac{N}{m} + .00209\frac{N}{m} = .00891\frac{N}{m} \tag{26}$$

A spiral placed in layers 3 or 4 of SUMMiT-V^{TM} would be 2.25 μm thick [6,31] with a linear stiffness of .01065N/m.

REFERENCES

1. Liu, C., 2006, *Foundations of MEMS*, Pearson/Prentice Hall, Upper Saddle River, NJ.

2. Madou, M., 2002, *Fundamentals of Microfabrication: The Science of Miniaturization*, CRC Press LLC., Boca Raton.

3. Burgess, S., Moore, D., Newland, D., and Klaubert, H., 1972, “A Study of Mechanical Configuration Optimization in Micro-systems,” Research in Engineering Design, **54**(3), pp. 507-539.

4. Pister, K., Judy, M., Burgett, S., and Fearing, R., 1992, “Microfabricated Hinges,” Sensors and Actuators A: Physical, **14** pp. 249-256.

5. Sandia National Labritories, 2008, “University Alliance - Design Competition,” from http://mems.sandia.gov/ua/contest.html

6. “SUMMiT-V™ Five Level Surface Micromachining Technology Design Manual”, 2008, from http://mems.sandia.gov/samples/doc/SUMMiT_V_Dmanual.pdf

7. Jensen, K., 2003, “Analysis and Design of Surface Micromachined Micromanipulators for Out-of-Plane Micropositining,” M.S. thesis, Brigham Young University, Provo, UT.

8. Hogan, A., 2010, “SEM Actuation of a Substrate Hinge” Experimental data not published, University of Utah, Salt Lake City, UT.

9. Zhang, W., Meng, G., and Chen, D., 2007, "Stability, Nonlinearity and Reliability of Electrostat8iically Actuated MEMS Devices," Sensors, **7**(5), pp. 760-796.

10. Spengen, W., Pures, R., and Wolf, I., 2006, "A Physical Model to Predict Stiction in MEMS," Journal of Micromechanics and Microengineering, **12**(5), pp. 189.

11. Baker, B., Hogan, A., 2010, “SEM Actuation of a Electroscope” Experimental data not published, University of Utah, Salt Lake City, UT.

12. Boutte, R., Horn, J., Gaskin, N., Meacham, T., Harvey, I., and Baker, B., 2006, "Deployable Hoberman-style Linkage," Sandia University Alliance Design Competition, University of Utah, Salt Lake City, UT.

13. Boutte, R., Horn, J., Gaskin, N., Meacham, T., Baker, B., and Harvey, I., 2005, "Invention Disclosure: Silicon-Based Microdeployable Structures," University of Utah: U-4120, University of Utah, Salt Lake City, UT.

14. Boutte, R., 2007, "Design of a Micro-Camera Using a Silicon Based Closed-Loop Micro-Deployable Structure," M.S., thesis, University of Utah, Salt Lake City, UT.

15. Meacham, T., 2007, "Microaperture Design," Sandia University Alliance Design Competition, University of Utah, Salt Lake City, UT.

16. Howell, L., 2001, *Compliant Mechanisms*, Wiley and Sons Inc., New York, NY.

17. Kota, S., Joo, J., Li, Z., Rodgers, S., and Sniegowski, J., 2001, "Design of Compliant Mechanisms: Applications to MEMS," Analog Integrated Circuits and Signal Processing, **29,** pp. 7-15.

18. Smith, E., and Lefebvre P., 1996, "PF16 Encodes a Protein with Armadillo Repeats and Localizes to a Single Microtubule of the Central Apparatus in *Chlamydomonas* Flagella," J. Cell Biology, **132**(3) pp.359-370, from http://remf.dartmouth.edu/images/algaeSEM/source/2.html

19. Witman, G., Carlson, K., Berliner, J., and Rosenbaum, J., 1972, "Isolation and Electrophoretic Analysis of Microtubules, Matrix, Membranes and Mastigonemes," J Cell Biol, **54**(3), pp. 507-539.

20. Cook, D., and Young, W.,1999, *Advanced Mechanics of Materials Second Edition*, Prentice Hall, Upper Saddle River, NJ, Chap. 4.

21. Awatar, S., Slocum, A., and Sevincer, E., "Characteristics of Beam-based Flexure Modules," ASME Journal of Mechanical Design, **129**(6), pp. 625-639.

22. Pei, X., Yu, J., Zong, G., and Bi, S., 2010, "An Effective Pseudo-rigid Body Method for Beam Based Compliant Mechanisms," Precision Engineering, **34**(3), pp.634-639.

23. Pai, P., 2007, *Highly Flexible Structures*, Aiaa, Blacksburg, VA.

24. Cook, R., Malkus, D., and Plesha, M., 1989, *Linear Concepts and Applications of Finite Element Analysis*, John Wiley, Hoboken, NJ.

25. Kreyszig, E., 2006, *Advanced Engineering Mathematics,* John Wiley, Hoboken, NJ, Chap. 8.

26. Kounadis, A., and Kratzig,W.,1995, *Nonlinear Stability of Structures Theory and Computational Techniques*, CISM Udine, Italy.

27. Harvey, I., 2007, “A SUMMiT^{TM}-Based MEMS Design for in-SEM Actuation, A Qualitative Proof-of-Concept for Dynamic MEMS Outreach Demonstrations,” Sandia University Alliance Design Competition, University of Utah, Salt Lake City, UT.

28. Harvey, I., Meacham, T., Harvey, I., E., Baker, B., 2007, “University of Utah Invention Disclosure with Filed Provisional Patent: U-4227 High-Force,” Non-Contact MEMS Actuation by Differential E-beam Charge Injection, University of Utah, Salt Lake City, UT.

29. Lobontiu, N., Garcia, E., and Canfield, S., 2004, “Torsional Stiffness of Several Variable Rectangular Cross-section Flexure Hinges for Macroscale and MEMS Applications,” Smart Materials and Structures, **13***,* pp. 12-19.

30. Wolter, A., Schenk, H., Korth, H., and Fraunhofer, H., “Torsional Stress, Fatigue and Fracture Strength in Silicon Hinges of a Micro Scanning Mirror,” Reliability, Testing, and Characterization of MEMS/MOEMS III SPIE, **5343,** pp.176-185.

31. Sniegowski, J., and Boer, M., “IC- Compatible Polysilicon Surface Micromachining,” Annual Review of Material Science, **30**(1), pp.299-333.

32. Ford, K., Hogan, A., 2010, “SEM Actuation of a Plate,” Experimental data not published, University of Utah, Salt Lake City, UT.

33. Baker, B., 2010, “Slider Rail Experiment,” University Alliance Novel Design Chip, Not published, University of Utah, Salt Lake City, UT.

34. Lusk, S., and Howell, L., 2008, “Spherical Bistable Micromechanism,” Journal of Mechanical Design, **130**(4), pp.124-130.

35. Friedberger, A., and Muller, R., 2002, "Improved Surface-micromachined Hinges for Fold-out Structures," Journal of Microelectromechanical Systems, **7**(3), pp. 315-19.

36. Baker, M., 2010, “Symmetric Elastic Hoop Script” ANSYS Beam 188 element, Scrip published here, University of Utah, Salt Lake City, UT.

37. Rezaiee-Pajand, M., and Alamatian, J., 2010, “The Dynamic Relaxation Method Using New Formulation for Fictitious Mass and Damping,” Structural Engineering and Mechanics, **34**(1), pp.109-133.

38. Baker, B., 2010, “Bistable Elastic Hoop Experiment,” Results published here, University of Utah, Salt Lake City, UT.

39. Ford, K., Fisher, C., Kempe, E., Lin, K., Baker, B., and Harvey, I., 2010, “MEMS Bistable Elastic Ring,” Sandia University Alliance Design Competition, University of Utah, Salt Lake City, UT.

40. Baker, B., 2010, “Compliant Rotation to Radial Motion Transducer Experiment,” Results published here, University of Utah, Salt Lake City, UT.

41. Brumbaugh, S., “Spiral Spring Actuator”, 2008 Sandia University Alliance, University of Utah, Salt Lake City, UT.

42. COMSOL AB, 2005, *COMSOL Multiphysics Structual Mechanics Guide. 3.2rd ed.*, COMSOL, Stockholm.

43. Okamoto, S., Shimamoto, N., Matsushita, Y., Fujita, T., Maenaka, K., and Takayama Y., 2006, “Large Deflection Electrostatic Spiral Actuator with Twisted-beams,” Transactions of the Institute of Electrical Engineering of Japan, **126**(7), pp. 286-291.

44. Fukushige, T., Hata, S., and Shimokohbe, A., 2005, “A MEMS Conical Spring Actuator Array,” Journal of Microelectromechanical Systems, **14**(2), pp. 243-253.

45. Zengatao, L., Myongseob, K., Nick, S., and Kan, E., 2005, “Actuation By Electrostatic Repulsion By Nonvolatile Charge Injection,” Sensors and Actuators A: Physical, **119**(1), pp. 236-234.

46. He, S., and Ridha, B.,”Design, Modeling, and Demonstration of a M-Force Out-Of-Plane Electrostatic Micro Actuator,” Journal of Microelectromechanical Systems, **17**(3), pp. 540-547.

47. Qiao, D.,Yuan, W., and Li, X., 2006, “Design of an Electrostatic Repulsive-Force Based Vertical Micro Actuator,” *Nano/Micro Engineered and Molecular Systems*, NEMS 1st IEEE International Conference.

48. He, S., and BenMrad, R., 2005, “Large-Stroke Microelectrostatic Actuators for Vertical Translation of Micromirrors used in Adaptive Optics,” IEEE Trans. Ind. Electron, **52**(4), pp. 974-983.

49. Lee, K., and Cho, Y., 2001, “Laterally Driven Electrostatic Repulsive-Force Microactuators Using Asymmetric Field Distribution,” Journal of Microelectromechanical Systems, **10**(1), pp. 128-136.

50. Harvey, I., 2009, "MEMS ChargePump - Mechanical Engineering - University of Utah," University of Utah, Salt Lake City, UT, from http://www.youtube.com/watch?v=BqCP9mQ7XCg

51. Ecsedy, K., Harvey, I., Hogan, A., Ford, K., Baker, B., Stout, P., Brumbaugh, S., and Piatt, J., 2010, “An Exploration of the Artistic Applications of MEMS: Gallery on a Chip,” The International Journal of Technology, Knowledge and Society, **6**(1), pp. 139-152.

52. Alsem, D., Hulst, R., Stach, E., Dugger, M., Hosson, J., and Ritchie, R., 2010, "Wear Mechanisms and Friction Parameters for Sliding Wear of Micron-Scale Polysilicon Side Walls," Sensors and Actuators A: Physical, **17**(5), pp. 373-382.

53. Walvern, J., 2003, "Failure Mechanisms in MEMS," *International Test Conference,* pp. 828-833.

54. Romig, A., Dugger, M., and McWhorter, P., 2003, “Materials Issues in Microelectromechanical Devices: Science, Engineering, Manufacturability and Reliability,” Acta Materialia*,* **51**(19) pp. 5837-5866